

**Two-way coupling model for wave-induced oscillatory soil response around marine structures**

Author

Zhai, H, Jeng, DS

Published

2022

Journal Title

Ocean Engineering

Version

Submitted Manuscript (SM)

DOI

[10.1016/j.oceaneng.2022.110791](https://doi.org/10.1016/j.oceaneng.2022.110791)

Rights statement

© 2022 Elsevier. Licensed under the Creative Commons Attribution-NonCommercial-NoDerivatives 4.0 International Licence (<http://creativecommons.org/licenses/by-nc-nd/4.0/>) which permits unrestricted, non-commercial use, distribution and reproduction in any medium, providing that the work is properly cited.

Downloaded from

<http://hdl.handle.net/10072/417167>

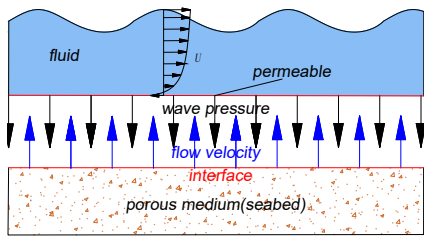
Griffith Research Online

<https://research-repository.griffith.edu.au>

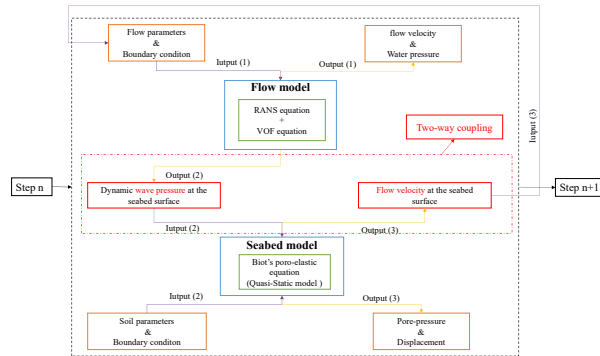
# 1 Graphical Abstract

## 2 Two-way coupling model for wave-induced oscillatory soil response around marine structures

3 Hualing Zhai<sup>1</sup> and Dong-Sheng Jeng<sup>2, #</sup>



(a) Concept of two-way coupling model



(b) Flowchart of the model

## 5 Highlights

### 6 **Two-way coupling model for wave-induced oscillatory soil response around marine struc-** 7 **tures**

8 Hualing Zhai<sup>1</sup> and Dong-Sheng Jeng<sup>2,#</sup>

- 9 • A new wave-seabed interaction model by two-way coupling algorithm is established in  
10 OpenFOAM.
- 11 • The combined velocity of seepage and soil displacement is introduced as the boundary  
12 for flow model.
- 13 • Seabed response from the two-way coupling model is smaller than that of the conven-  
14 tional models.
- 15 • The two-way coupling algorithm is necessary for evaluation of sediment motion and scour  
16 process.
- 17 • Effects of the two-way coupling process will be more significant for the cases with a  
18 structure.

# Two-way coupling model for wave-induced oscillatory soil response around marine structures

Hualing Zhai<sup>1</sup>  and Dong-Sheng Jeng<sup>2,#</sup> 

<sup>1</sup> School of Civil Engineering, Southwest Jiao Tong University, Chengdu 610031, China

<sup>2</sup> School of Engineering & Built Environment, Griffith University Gold Coast Campus, Queensland 4222, Australia

# Corresponding author.

---

## Abstract

Considerable efforts have been devoted to the topic of wave-seabed interactions in the last two decades because of growing offshore activities. The existing studies have based on one-way coupling approach. In this study, a new two-way coupling algorithm is proposed to overcome the contradiction at the fluid-sediment interface between physical process and the existing theoretical models. The numerical results indicates that the seabed responses obtained by the two-way coupling model are slightly lower than that of the one-way coupling model. However, the two-way coupling model significantly affects the Shields number that would further affect the scour process. Parametric analysis indicates that larger wave height, current velocity and soil permeability and smaller water depth, shear modulus and saturation degree would increase the difference of two coupling algorithms. Meanwhile, the difference between two coupling algorithms is significant around the mono-pile and dumbbell cofferdam, compared with the case without a structure.

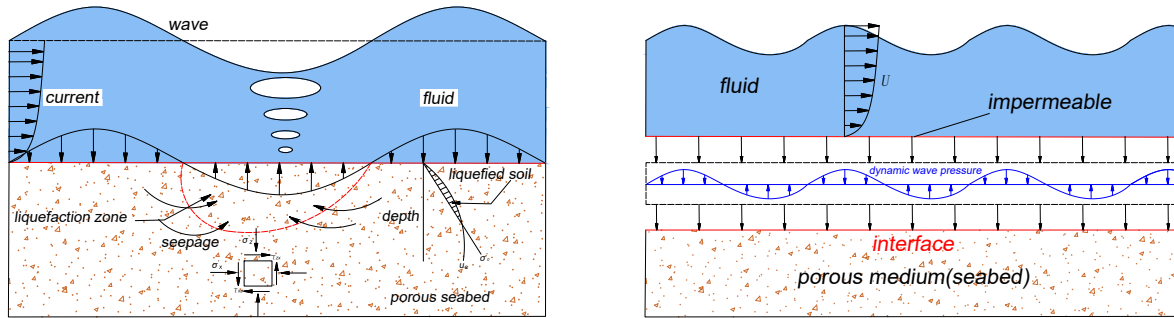
*Keywords:* Two-way coupling algorithm; wave-seabed interaction; pore pressures; pile foundation; dumbbell cofferdam

---

## 1. Introduction

The problem of the wave-seabed interactions around a marine structure has become an important issue in the field of coastal geotechnical engineering, due to the exploitation of marine resources and construction of marine infrastructures (Sumer, 2014; Jeng, 2018; Alcérrecas-Huerta and Oumeraci, 2018; Liu et al., 2020). In general, dynamic wave pressures acting on the seabed surface will cause significant variations of the pore pressures and stresses within

35 a porous seabed, which may further lead to seabed instability such as liquefaction around the  
 36 foundations of marine infrastructures, as illustrated in Figure 1(a). This engineering problem  
 37 consists of two domains, flow and seabed domains.



(a) problem of wave-seabed interactions

(b) one-way coupling concept

Figure 1: (a) Sketch of wave-seabed interactions, and (b) concept of one-way coupling process.

38 Most existing theoretical models (both analytical solutions and numerical simulations) for  
 39 wave-seabed interactions have based on one-way coupling (or named as integrated) process  
 40 (Jeng et al., 2013). In these approaches, the flow domain is solved by either potential flow  
 41 (Yamamoto et al., 1978; Hsu and Jeng, 1994) or Navier-Stokes model (Jeng et al., 2013; Yang  
 42 and Ye, 2017; Li et al., 2018, 2020a), which assumed that an impermeable seabed as the bottom  
 43 boundary condition, as shown in Figure 1(b). Based on the flow model for wave motion with  
 44 (or without) currents, the dynamic wave pressures along the seabed surface can be obtained  
 45 and used as the external loading for the seabed domain, which is a porous medium. There is  
 46 an obvious contradiction between the physical process and theoretical models in the existing  
 47 approaches. That is, the assumption of the impermeable seabed for flow model contradicts the  
 48 porous seabed model. Another drawback of the one-way coupling or integrated models is that  
 49 wave motion will not be affected by the seabed characteristics such as deformation and seepage,  
 50 although it may not always be significant for certain types of seabeds.

51 To overcome the above contradiction between physical process and theoretical models, two  
 52 methods can be adopted. The first approach is to solve flow and seabed at the same time in  
 53 one model, which ensures fluid and solid domains neither detach nor overlap during deforma-  
 54 tion (Zhang and Hisada, 2001). However, the method requires a large system equation consist

---

55 of discrete equations of fluid and seabed domains, which would likely cause the instability of  
56 the numerical results due to the large difference of fluid and seabed stiffness. Meanwhile, the  
57 method requires the same mesh along the interface of wave and seabed, which is difficult in  
58 practice due to the same accuracy usually requiring larger mesh size of fluid domain compar-  
59 ing with the seabed fluid (Wang et al., 2004). Another approach is to solve flow and seabed  
60 separately, but the data exchange the boundary conditions at the interface of wave and seabed  
61 domains would be bidirectional rather than one-way. This could avoid the demerits of the first  
62 method and allowed the spatial distributions of nodes along the interface and the time-step size  
63 in different sub-domains.

64 At the early stage of the theoretical development of the wave-induced soil response, the  
65 linear wave theory (Dean and Dalrymple, 1984) was adopted to obtain analytical solutions.  
66 Based on Biot's poro-elastic theory (Biot, 1941), Yamamoto et al. (1978) and Madsen (1978)  
67 were two classic publications for an infinite seabed under two-dimensional wave loading. The  
68 same framework has been further extended to three-dimensional short-crested wave system in  
69 an-isotropic seabed (Hsu et al., 1993; Hsu and Jeng, 1994; Jeng and Hsu, 1996; Hsu et al.,  
70 1995; Tsai, 1995), a cross-anisotropic seabed (Jeng, 1997), or non-homogeneous seabed (Jeng  
71 and Seymour, 1997; Kitano and Mase, 1999). Another approach based on the mixture theory,  
72 Mei and Foda (1981) proposed a boundary-layered approximation for wave-induced seabed  
73 response, which provide sufficient accuracy for the prediction of the wave-induced soil lique-  
74 faction (Hsu and Jeng, 1994).

75 In addition to analytical solutions, numerous numerical studies for the wave-seabed interac-  
76 tions have been available in the literature. Among these, Gatmiri (1992) proposed a FEM model  
77 to investigate the wave induced pore-pressures and effective stresses of poro-elastic seabeds, in  
78 which the linear sinusoidal wave was adopted. Later, a one-dimensional FEM has been pro-  
79 posed to investigate the wave-induced seabed response with variable permeability and shear  
80 modulus (Jeng and Lin, 1996). Later, Liu and Garcia (2007) established the fluid-seabed inter-  
81 action numerical model by finite volume method (FVM) to investigate the seabed response and  
82 the coupling between fluid and seabed was through stress and continuity condition on common  
83 boundaries. Recently, several numerical studies for the wave-induced dynamic seabed response  
84 around various offshore infrastructures have been carried out by one-way coupling (or called

---

85 integrated model) with different seabed models (Jeng et al., 2013; Ye et al., 2014, 2015; Zhao  
86 and Jeng, 2015; Ye et al., 2016; Zhao et al., 2020; Zhang et al., 2011; Ye et al., 2021; Cui et al.,  
87 2021; Cui and Jeng, 2021).

88 The open source code (OpenFOAM) has been recently used as one of CFD models for the  
89 numerical simulation in the field of coastal engineering. Elsafti and Oumeraci (2016, 2017)  
90 developed a solver named "geotechFoam" in OpenFOAM to simulate soil-structure-interaction  
91 for marine gravity structures and five benchmark cases and two sets of physical model tests  
92 were applied for the validation. Lin et al. (2017) proposed an integrated OpenFOAM solver for  
93 wave-seabed-structure interactions to investigated nonlinear wave-induced seabed response and  
94 associated momentary liquefaction around mono-pile foundation. Later, Li et al. (2020b) im-  
95 plemented an open-source numerical toolbox for modeling the seabed response with waves and  
96 structures based OpenFOAM framework and performed two-dimensional (2D) nonlinear wave-  
97 seabed interaction and three-dimensional (3D) wave-induced seabed response around offshore  
98 foundations. More detailed review for the OpenFOAM model for wave-seabed-structure inter-  
99 actions can be found in Diaz-Carrasco et al. (2021).

100 All the aforementioned studies have adopted the one-way coupling approach (or named  
101 integrated model). To date, only a few researchers attempted the two-way coupling approach to  
102 understand in the effects of seabed characteristics on the wave motion, such as wave damping  
103 effects. For example, Jeng (2000) adopted the analytical solution for the seabed model (Hsu and  
104 Jeng, 1994) with the concept of complex wave number to examine the wave damping process.  
105 However, his approach was based on the linear wave theory and potential flow theory. This  
106 approach was further extended to wave-seabed interaction in a Coulomb-damped seabed (Lee  
107 et al., 2002). Wang et al. (2004) proposed a weak coupling algorithm for the wave-seabed  
108 interaction, based on the error integration over a time interval and space along fluid-seabed  
109 interfaces. Their model exchanged the pressure and normal velocity at the seabed surface but  
110 ignored the velocity in other direction. In their study (Wang et al., 2004), the fluid domain  
111 was solved by FVM, while the seabed was solved by meshfree model. Later, Karunarthna and  
112 Lin (2006) proposed a two-way coupling algorithm for both wave and seabed fields by the N-S  
113 equation for wave field and Biot's QS equations for the pore pressures in the seabed domain.  
114 However, in their model, the seabed was regarded as a porous medium as fluid seepage through,

---

115 but they ignored the effective stress and soil displacements.

116 In this study, a new two-way coupling algorithm for the wave–seabed interfaces will be pro-  
117 posed. Within the OpenFOAM source code, the existing OpenFOAM model for fluid-seabed-  
118 structure interactions (PORO-FSSI-FOAM, (Liang and Jeng, 2021)) will be further improved  
119 by including the concept of the two-way coupling approach. In the present model, the assump-  
120 tion of impermeable seabed in the existing OpenFOAM model will be released and introducing  
121 the continuity of fluid velocity incorporating with seepage velocity and velocity due to soil dis-  
122 placements obtained from the seabed model. In this approach, wave and seabed models will be  
123 fully coupled, and the effects of seabed characteristic on the wave motion can be integrated. The  
124 proposed model was validated by the previous analytical solutions and experimental data. The  
125 present two-way coupling algorithm will be compared with the previous one-way coupling al-  
126 gorithm (Liang and Jeng, 2021). The effects of two-way coupling approach on fluid and seabed  
127 field characteristics was investigated through a parametric study. Based on the present model,  
128 we further consider two marine structures as engineering applications of the proposed model,  
129 including offshore mono-piles and dumbbell cofferdam.

## 130 **2. Theoretical Models**

131 In this study, the one-way integrated model, PORO-FSSI-FOAM, developed by Liang et al.  
132 (2020) is further implemented for the present two-way coupling model. The present model con-  
133 sists of two main sub-models: flow and seabed models. The flow model was based on the exist-  
134 ing OpenFOAM model (IHFOAM or olaFlow) (Higuera et al., 2013), while the porous seabed  
135 model was based on Biot’s poro-elastic theory (Liang et al., 2020). In these two sub-models,  
136 we make an implement to introduce a coupling process to link seabed and wave components,  
137 which is the main contribution of this study. In this section, the governing equations and bound-  
138 ary conditions of the fluid-seabed interactions are outlined. Details of the numerical flow and  
139 seabed models can refer to Liang et al. (2020). We will focus on how the two-way coupling  
140 concept be adopted in the existing model.

---

141 2.1. Governing equations

142 2.1.1. Flow model

143 The RANS(Reynolds Average Navier-Stokes) equations are adopted to calculate the in-  
144 compressible fluid field for the two-way coupling model based on conservation of mass and  
145 momentum, which are outlined as (Higuera et al., 2013; Li et al., 2020b; Liang et al., 2020):

$$\nabla \cdot \mathbf{u}_f = 0, \quad (1a)$$

$$\frac{\partial \rho_w \mathbf{u}_f}{\partial t} + \rho_w (\mathbf{u}_f \cdot \nabla) \mathbf{u}_f = -\nabla p_w + \nabla \cdot \tau + \rho_w \mathbf{g}, \quad (1b)$$

146

147 in which  $\mathbf{u}_f$  is the fluid velocity vector;  $p_w$  is the fluid pressure;  $\mathbf{g}$  is the body force vector;  $t$  is  
148 time and  $\tau$  is the viscous stress tensor with Einstein notation of  $\tau_{ij}$ . For Newtonian fluid,

$$\tau_{ij} = \mu \left( \frac{\partial u_i}{\partial x_j} + \frac{\partial u_j}{\partial x_i} \right), \quad (2)$$

149 where  $\mu$  is the dynamic molecular viscosity with  $\mu_{air}$  and  $\mu_{water}$  for the air and water, respec-  
150 tively;  $u_i$  and  $u_j$  ( $i, j \in [1,2,3]$ ) donate the velocity components in the  $x$ -,  $y$ - and  $z$ - directions,  
151 respectively.

152 In order to describe the phenomenon of wave propagation and trace the free surface, the  
153 volume of fluid (VOF) method (Hirt and Nichols, 1981) was taken into account. The governing  
154 equation of VOF method is described as:

$$\frac{\partial \alpha}{\partial t} + \nabla \cdot (\alpha \mathbf{u}_f) + \nabla \cdot [\alpha(1 - \alpha) \mathbf{u}_r] = 0, \quad (3)$$

155 in which  $\mathbf{u}_r$  is the relative velocity field,  $\alpha$  represents the quantity of water per unit volume of  
156 each cell and  $(1 - \alpha)$  indicates the volume fraction of air:

$$\alpha = \begin{cases} 1, & \text{water,} \\ 0, & \text{air,} \\ 0 < \alpha < 1, & \text{free surface.} \end{cases} \quad (4)$$

157 More detailed mathematical derivations for the flow model (olaFlow) can be found in [Higuera](#)  
 158 [et al. \(2013\)](#).

### 159 2.1.2. Porous seabed model

160 The seabed was considered as a porous elastic material composed of pore-fluid and soil  
 161 skeleton, as described by Biot's quasi-static (QS) model ([Biot, 1941](#)). The governing equation  
 162 for the soil behavior of the two-dimensional problem can be written as:

$$k_s \nabla^2 p_s - n_s \beta_s \gamma_w \frac{\partial p_s}{\partial t} = \gamma_w \frac{\partial(\nabla \cdot \mathbf{u}_s)}{\partial t}, \quad (5a)$$

$$G_s \nabla^2 \mathbf{u}_s + \frac{G_s}{1 - 2\mu_s} \frac{\partial(\nabla \cdot \mathbf{u}_s)}{\partial x} = \nabla p_s, \quad (5b)$$

163  
 164 in which  $\nabla^2 (= \frac{\partial^2}{\partial x^2} + \frac{\partial^2}{\partial y^2} + \frac{\partial^2}{\partial z^2})$  is the Laplace operator;  $p_s$  is the pore pressure;  $n_s$  is the soil  
 165 porosity;  $k_s$  is the soil permeability;  $\mathbf{u}_s = (u_s, v_s, w_s)$  is the soil displacement vector;  $G_s$  is the  
 166 shear modulus and  $\beta_s$  is the compressibility of the pore fluid, which is defined as ([Verruijt, 1969](#)),

$$\beta_s = \frac{1}{K'} = \frac{1}{K_w} + \frac{1 - S_r}{P_{w0}}, \quad (6)$$

167 where  $K_w$  is the true bulk modulus of the elasticity of water, which may be taken as  $2 \times 10^9 \text{ N/m}^2$   
 168 ([Yamamoto et al., 1978](#)), and  $P_{w0}$  represents the absolute pore-pressure.

169 Based on generalized Hooke' law, the relationship between soil displacements and effective  
 170 normal stress and shear stress can be expressed as:

$$\begin{bmatrix} \sigma'_x \\ \sigma'_y \\ \sigma'_z \\ \tau_{xz} \\ \tau_{xy} \\ \tau_{yz} \end{bmatrix} = G_s \begin{bmatrix} C_1 & C_2 & C_2 & 0 & 0 & 0 \\ C_2 & C_1 & C_2 & 0 & 0 & 0 \\ C_2 & C_2 & C_1 & 0 & 0 & 0 \\ 0 & 0 & 0 & 1 & 0 & 0 \\ 0 & 0 & 0 & 0 & 1 & 0 \\ 0 & 0 & 0 & 0 & 0 & 1 \end{bmatrix} \begin{bmatrix} \frac{\partial u_s}{\partial x} \\ \frac{\partial v_s}{\partial y} \\ \frac{\partial w_s}{\partial z} \\ \left(\frac{\partial u_s}{\partial z} + \frac{\partial w_s}{\partial x}\right) \\ \left(\frac{\partial u_s}{\partial y} + \frac{\partial v_s}{\partial x}\right) \\ \left(\frac{\partial v_s}{\partial z} + \frac{\partial w_s}{\partial z}\right) \end{bmatrix} \quad (7)$$

---

171 where  $C_1 = 2(1 - \mu_s)/(1 - 2\mu_s)$  and  $C_2 = 2\mu_s/(1 - 2\mu_s)$ . Note that a positive sign is taken as a  
172 compressive stress considered in this study.

173 In general, there are three different approaches for Biot's poro-elastic theory (Biot, 1941,  
174 1956a,b). They are: quasi-static (so-called consolidation model),  $u - p$  partially dynamic model  
175 and full dynamic model. The  $u - p$  approximation or fully dynamic models for wave-seabed  
176 interactions have been intensive studied by numerous researchers (Jeng and Rahman, 2000;  
177 Jeng and Cha, 2003; Ulker et al., 2009). According Jeng and Cha (2003) and Ulker et al.  
178 (2009), the input data used in numerical examples are in the applicable range of quasi-static  
179 model. Therefore, to simplify the numerical coding, we use the quasi-static model as the first  
180 approximation. For the  $u - p$  approximation or full dynamic model with the concept of two-way  
181 coupling approach will be developed in the future.

## 182 2.2. Boundary conditions

183 The boundaries of fluid field in the flow sub-model include inlet and outlet of flow, atmo-  
184 spheric boundary, two lateral boundaries at both side and the bottom of fluid. The progressive  
185 wave is generated in the inlet of the model with various wave theories. An active wave ab-  
186 sorption model is employed in outlet condition to eliminate reflected waves. A pressure outlet  
187 condition is adopted in the atmospheric boundary. For the lateral sides boundary, a rigid wall  
188 boundary with a no-slip condition is imposed and the velocity is regarded as zero.

189 Unlike previous flow-sub model (Higuera et al., 2013; Liang et al., 2020; Liang and Jeng,  
190 2021), in the present model, the bottom boundary condition of flow sub-model treated as per-  
191 meable wall with the fixed value, which is obtained from the combined seepage velocity and  
192 soil displacement induced velocity:

$$\mathbf{u}_f = -\frac{k_s}{\gamma_w} \nabla p_s + \frac{\partial \mathbf{u}_s}{\partial t}, \quad \text{at } z = 0. \quad (8)$$

193 Note that the above boundary condition is similar to those in Jeng (2000) and Wang et al. (2004).  
194 However, Wang et al. (2004) missed out a negative sign in the first-term of the right-hand-side,  
195 which could be a typo. Note that the first term on the right-hand-side of (8) is the wave-induced  
196 seepage velocity and the second term represents the velocity due to soil displacements. At the  
197 seabed surface, the fluid velocity in the fluid domain should be matched with the combined

---

198 velocity of seepage of pore-fluid and velocity of solid particle. With this boundary condition,  
199 the effects of seabed characteristics on the wave motion can be examined.

200 For the porous seabed model, the boundaries of seabed domain include the interface between  
201 fluid and seabed, the bottom and four lateral sides. A impermeable fixed boundary is adopted to  
202 describe the bottom and lateral sides. Hence, the soil displacements and pore-pressure gradient  
203 are regarded as zero.

$$u_s = v_s = w_s = \frac{\partial p_s}{\partial \mathbf{n}} = 0, \quad (9)$$

204 where  $\mathbf{n}$  is the normal vector of the boundary.

205 At the seabed surface, the dynamic water pressures are equal to the pore pressures, while  
206 the vertical effective stresses and shear stress are vanished.

$$p_s(x, y, z, t) = p_w(x, y, z, t), \quad \sigma'_z = \tau_{xz} = \tau_{yz} = 0. \quad (10)$$

207 Note that the shear stresses are set as zero at the seabed surface, because it is small compared  
208 with the dynamic wave pressures in shallow water. The effects of wave shear stress on the  
209 wave-induced soil response was investigated by [Ye and Jeng \(2011\)](#).

### 210 2.3. *Concept of two-way coupling process*

211 The aim of including the two-way coupling algorithm in the wave–seabed interaction model  
212 is to reflect the mutual influence of the two sub-model. The sketch of two-way coupling algo-  
213 rithm is represented in Figure 2. As mentioned previously, the main contradiction between the  
214 physical process and previous integrated model lies on the assumption of impermeable seabed  
215 in the flow model. In this study, the impermeable seabed boundary condition for the flow model  
216 will be replaced by the continuity boundary condition of velocities. Similar with the one-way  
217 coupling algorithm, the hydrodynamic water pressure at the bottom of fluid domain is employed  
218 as one of boundary conditions along the seabed surface for the seabed model to investigate the  
219 influence of fluid characteristic on seabed response. Meanwhile, the permeable interface allows  
220 the existence of flow velocity, which is calculated by the seepage velocity and soil displacement  
221 induced velocity on seabed model, which is regarded as a form to reflect the influence of seabed  
222 response on fluid characteristics.

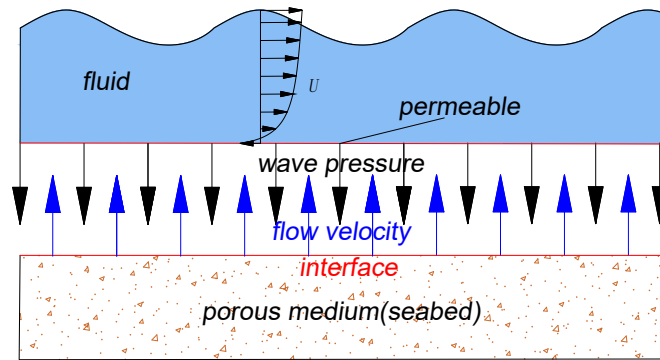


Figure 2: The concept of two-way coupling process in the present research.

223 **2.4. Coupling process**

224 In the present study, the whole loop from one time step to the next time step for the two-way  
 225 coupling algorithm in Figure 3 is divided into four steps:

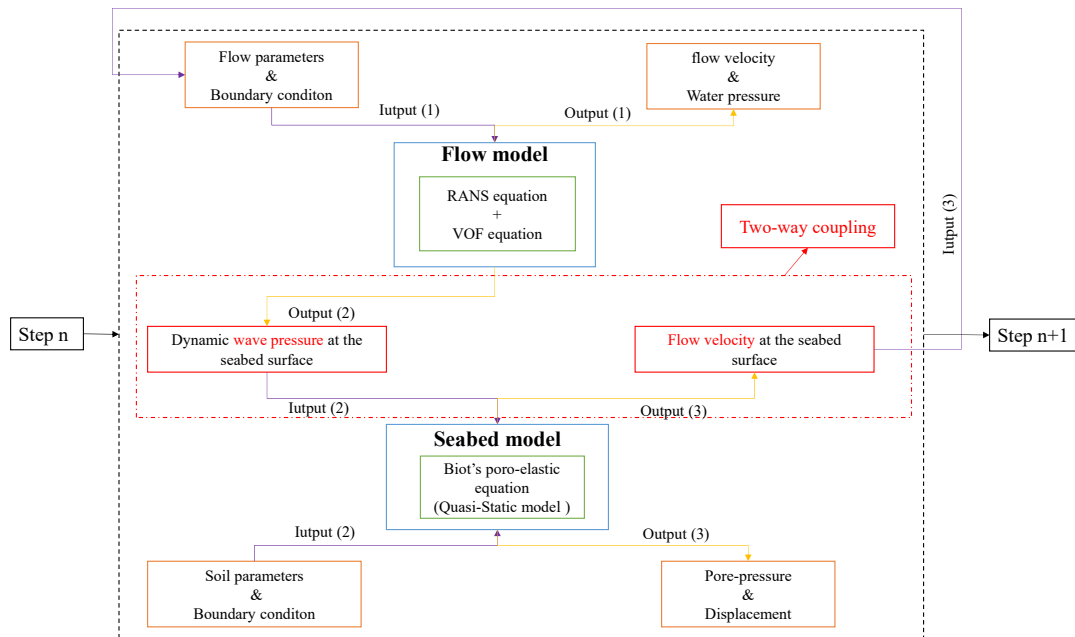


Figure 3: Flow chart of the numerical model.

- 226 • Steps 1: The flow parameters and boundary conditions are imported into flow model to  
 227 solve the water pressure and flow velocity of the whole computational domain. Then,

---

228 the dynamic wave pressure of the interface is imported as the external loading for the  
229 seabed model. Note that this step is the one-way coupling process, which is same as the  
230 previous model (Liang et al., 2020; Liang and Jeng, 2021). This is aim to obtain the initial  
231 condition for the flow domain, based on the assumption of impermeable seabed.

232 • Steps 2: With soil parameters and dynamic wave pressures from the wave model in Step 1,  
233 the pore pressures, stresses and soil displacements obtained in the porous seabed model.

234 • Steps 3: Now, we replace the boundary condition at the interface for the flow model  
235 by (8), in which the pore pressures and soil displacements are obtained from the seabed  
236 model in Step 2. In this boundary condition, the flow velocity caused by the combination  
237 of seepage velocity and movement of soil particle induced velocity at the interface is  
238 added as the boundary condition of flow model. Then, the fluid domain will be updated  
239 after running flow model.

240 • Step 4: The updated dynamic wave pressures will be used as the new external loading for  
241 the seabed model, and go to Step 2.

242 Noted that the at the beginning of the model ( $n = 1$  in Figure 3), the flow velocity at the  
243 interaction of fluid and seabed surface are set up as zero by setting the boundary conditions  
244 as "fixedValue" of zero. Hence, the numerical process of two-way coupling model is same as  
245 the one-way coupling model at the first time step. Then, the flow velocities at the interface are  
246 calculated and input to the flow model as boundary condition at the end of the first time step.  
247 Then the two-way coupling process as Figure 3 start from the second time step.

248 As seen in Figure 3 , With the output(3) from the seabed model, we can obtain the combined  
249 velocity due to seepage and soil particle at the fluid-seabed interface as Input(3) for the flow  
250 model. This will affect the flow domain at each time step. In the previous one-way coupling  
251 model, there is no Input(3) in the flow model, which cannot include the effects of soil properties  
252 in the flow model.

## 253 2.5. Numerical scheme

254 The two-way coupling model combine the RANS equation solver and QS equation solver to  
255 a system solver. The computational domain for the two-way coupling model is represented in

256 Figure 4, in which the fluid and seabed fluid are co-established. It is noted that a gap is occurs  
 257 between the fluid and seabed domain, which is necessary to realize the independent naming of  
 258 the fluid field bottom and seabed field surface, although the two boundaries describe the same  
 259 interface in physical process. Then, the data can be exchanged between the two boundaries to  
 260 realize the two-way coupling algorithm. Hence, the value of the gap is required to exist but not  
 261 specific value is required. In the paper, the value of the gap is selected as  $1 \times 10^{-6}$  m, which is  
 262 smaller enough compared with the grid size.

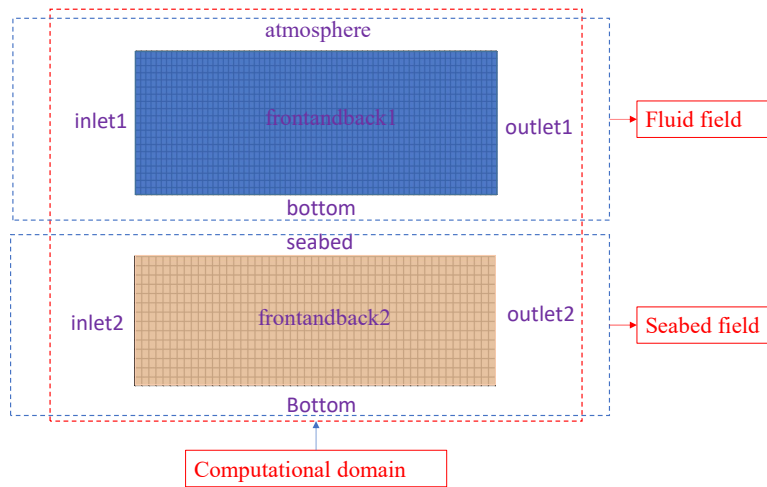


Figure 4: The computational domain and boundary name for the numerical model.

263 The boundary conditions for both flow and seabed models are given in Table 1, in which  
 264 the names and positions of the boundaries are given in Figure 4. As seen in the table, the  
 265 boundary conditions of water pressure ( $p$ ) and flow velocity ( $\mathbf{u}_f$ ) for seabed field (including  
 266 five boundaries of inlet2, outlet2, seabed, Bottom and frontandback2) are set as "fixedValue" of  
 267 zero when solving the RANS equation. Hence, the results of water pressure and flow velocity at  
 268 the seabed field are zero and only the water pressure and flow velocity at fluid fields are useful.  
 269 Similarly, the boundary conditions of pore-pressure( $p_s$ ) and soil displacement( $U_s$ ) for fluid field  
 270 are set as "fixedValue" of zero when solving the QS equation and the results of seabed response  
 271 on fluid field is useless. Finally, the water pressure and flow velocity in fluid field and pore-  
 272 pressure and soil displacement in seabed field are selected to realize the fluid-seabed interaction  
 273 model. The detailed numerical code of the two-way coupling process is given in Appendix A.

Table 1: Setting of boundary conditions for the numerical model.

	$p$	$\mathbf{u}_f$	$p_s$	$\mathbf{u}_s$
inlet1	fixedFluxPressure	waveVelocity	fixedValue	fixedValue
outlet1	fixedFluxPressure	waveAbsorption2Dvelocity	fixedValue	fixedValue
atmosphere	totalPressure	pressureInletOutVelocity	fixedValue	fixedValue
bottom	fixedFluxPressure	pressureInletOutVelocity	fixedValue	fixedValue
frontandback1	empty or fixedValue	empty or fixedValue	empty or fixedValue	empty or fixedValue
inlet2	fixedValue	fixedValue	zeroGradient	slip
outlet2	fixedValue	fixedValue	zeroGradient	slip
seabed	fixedValue	fixedValue	fixedValue	tractionDisplacement
Bottom	fixedValue	fixedValue	zeroGradient	slip
frontandback2	empty or fixedValue	empty or fixedValue	empty or zeroGradient	empty or slip

### 274 3. Validation of the numerical model

275 In this section, the numerical model will be validated by comparing the numerical results  
 276 with the laboratory experimental data and analytical solution available in the literature. The  
 277 following validations will be presented in this section.

- 278 • Validation #1: Comparison with the analytical solution (Hsu and Jeng, 1994) and experi-  
 279 mental data (Liu et al., 2015) for the pore pressure in vertical direction.
- 280 • Validation #2: Comparison with SWJTU laboratory experimental data of Wang et al.  
 281 (2019) for water pressures and pore-pressures around the mono-pile.

#### 282 3.1. Validation #1: Comparison with the analytical solution (Hsu and Jeng, 1994) and the 283 compressive test (Liu et al., 2015)

284 The first validation is comparison of the wave-induced pore pressure along with the seabed  
 285 depth ( $z/d_s$ ) between present two coupling models with the experimental data (Liu et al., 2015)  
 286 and the analytical solution (Hsu and Jeng, 1994). The following parameters were used in this  
 287 example, which are based on the experiments: wave height( $H$ ) = 3.5 m, water depth( $d$ )= 5.2 m,  
 288 wave period ( $T$ )= 9 s, seabed thickness ( $d_s$ )= 1.8 m, Poisson' ratio ( $\mu_s$ ) =0.3, soil permeability  
 289 ( $k_s$ ) =  $1.8 \times 10^{-4}$  m/s, Shear modulus ( $G_s$ ) =  $1.27 \times 10^7$  N/m<sup>2</sup>, porosity of seabed ( $n_s$ )=0.425 and  
 290 the degree of saturation ( $S_r$ ) = 99.6%.

291 The compared results of the maximum wave-induced pore pressure ( $|p_s|/p_0$ ) within the  
 292 seabed with depth ( $z/d_s$ ) were presented in Figure 5, in which  $p_s$  denotes the maximal pore  
 293 pressure and  $p_0(= \gamma_w H/2 \cosh kd)$  denotes the amplitude of linear wave induced dynamic wave  
 294 pressure at the seabed surface. It is obvious from the figure that the results of the present model  
 295 for one-way and two-way coupling algorithms all have the same trend with the analytical so-  
 296 lution (Hsu and Jeng, 1994). However, the  $|p_s|/p_0$  of present model obtained by one-way and  
 297 two-way coupling algorithms all larger than the analytical solutions near the seabed surface,  
 298 which was due to the given wave beyond the range of linear wave but the Hsu and Jeng (1994)  
 299 still used the linear wave theory. Meanwhile, the present model agrees well with the experimen-  
 300 tal data (Liu et al., 2015), but the results of two-way coupling model closer to the experimental  
 301 results comparing with the present one-way coupling model.

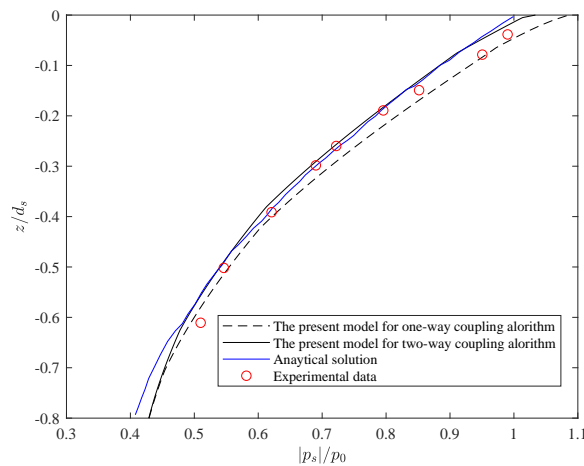


Figure 5: Comparisons of the present results by two coupling algorithms with the experimental data (Liu et al., 2015) and the analytical solution (Hsu and Jeng, 1994).

302 3.2. Validation #2: Comparison with the wave flume experiment for a mono-pile (Wang et al.,  
 303 2019)

304 The second validation is to compare the water pressure on the mono-pile and pore pressure  
 305 in the seabed of the present model with SWJTU laboratory experimental data (Wang et al.,  
 306 2019) around the mono-pile. The mono-pile was located in the center of sediment tanks and  
 307 the diameter was 0.3 m. The wave and seabed parameters in the experiments were adopted as:

308 wave height( $H$ ) = 0.12 m, water depth( $d$ )= 0.6 m, wave period ( $T$ )= 1.6 s, Poisson' ratio ( $\mu_s$ )  
 309 =0.3, soil permeability ( $k_s$ ) = $2.382 \times 10^{-5}$  m/s, Shear modulus ( $G_s$ )=  $8.58 \times 10^6$  N/m<sup>2</sup>, porosity  
 310 of seabed ( $n_s$ )=0.448 and seabed thickness ( $d_s$ )=1 m, and degree of saturation ( $S_r$ )=1).

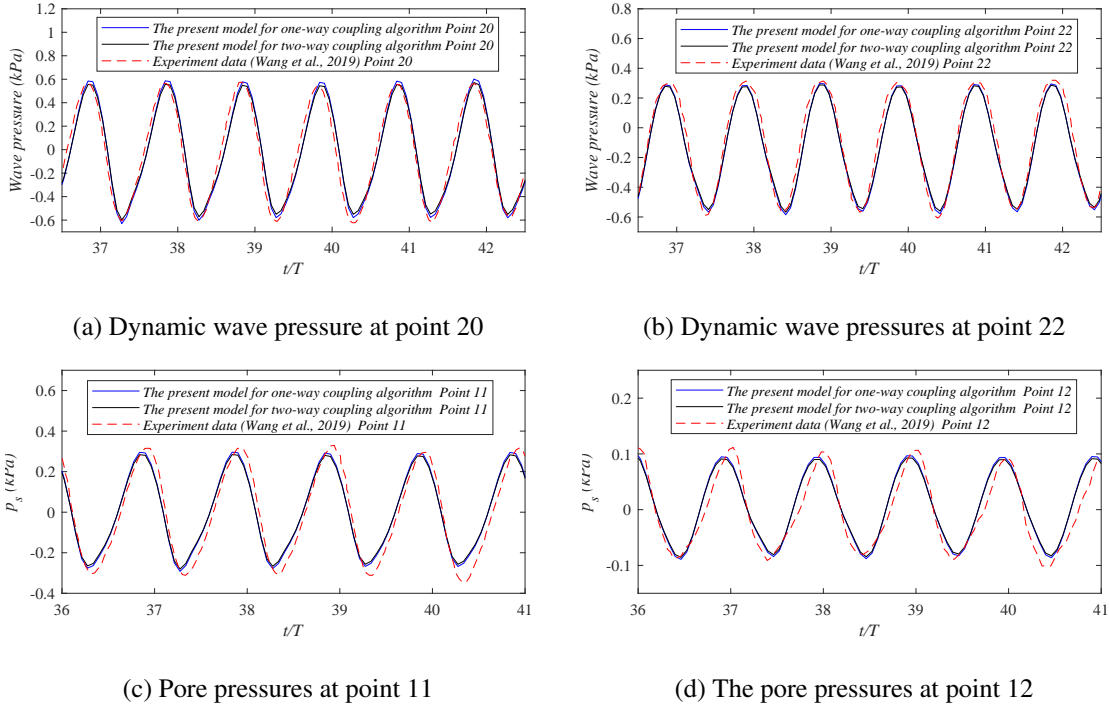


Figure 6: Comparisons of the present model for two different coupling algorithms and experimental data (Wang et al., 2019) for dynamic wave pressures on the mono-pile and pore pressures in the seabed around a pile under wave loading. (a) & (b) dynamic wave pressures at Points 20 & 22; and (c) & (d) pore-water pressures at Points 11 & 12.

311 The comparison of dynamic wave pressures and pore-pressures are plotted in Figure 6.  
 312 Herein, the dynamic wave pressure at point 20 and point 22 are presented in Figure 6(a) & (b),  
 313 respectively, in which point 20 and 22 were located beside and behind the pile of 0.4 m above  
 314 seabed surface, respectively. It is clear in the figure that the numerical results agrees well with  
 315 the experimental data (Wang et al., 2019). Meanwhile, the results of pore-pressures at points  
 316 11 & 12 are illustrated in Figure 6(c) & (d), respectively. Noted that points 11 & 12 were  
 317 located in the seabed of  $z/d_s = 0.05$  and  $0.15$  behind the pile. The comparison indicates that  
 318 the present model overall agrees with the experimental data (Wang et al., 2019). However, the  
 319 results obtained by one-way coupling model are slightly larger than that of two-way coupling  
 320 model but the difference are so small that can be ignored in the case.

---

321 **4. Comparison between two-way and one-way coupling models for 2D wave-seabed inter-**  
322 **actions**

323 In the section, we will compare the flow and seabed characteristics by using two-way with  
324 one-way coupling algorithms and clarify the condition when the two-way coupling model is  
325 necessary. Hence, a sandy bed is used in numerical examples and the flow velocity, pressures,  
326 soil displacements, stresses and Shields number are examined, which would impact the soil  
327 response. Figure 7 shows the sketch of the 2D problem of wave-seabed interactions. The  
328 coordinate system is established with seabed surface along the wave propagation direction as  
329 the  $x$ -axis and the  $z$ -axis is upward from the seabed surface ( $z = 0$ ). The length of computational  
330 domain ( $L_s$ ) is set as three times linear wavelength ( $L_0$ ), while  $d$  is the water depth and  $d_s$  is  
331 seabed thickness. The input parameters for numerical examples are given in Table 2. The  
332 friction coefficient of soil ( $f$ ) is determined by  $f = \tan \varphi$ , in which  $\varphi$  is the internal friction  
333 angle of soils. The range of  $\varphi$  for a sandy soil is about  $20^\circ$ – $40^\circ$ . In this study,  $30^\circ$  of the internal  
334 friction angle is selected for the sandy soils (Lube et al., 2004; Cha and Cho, 2007).

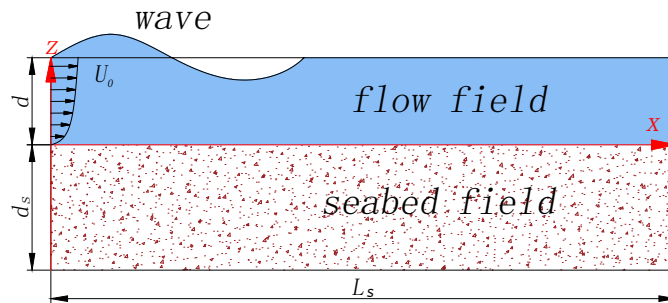


Figure 7: The sketch of the numerical model.

335 The essential difference between the one-way and two-way coupling algorithm is the dif-  
336 ferent assumption for the interface between fluid and seabed (i.e., the seabed surface). The  
337 interface of fluid and seabed is assumed as slip and impermeable in one-way coupling model,  
338 from which the flow velocity at the seabed surface is regarded as zero. This is common assump-  
339 tion used in the existing models for wave–seabed interactions (Yamamoto et al., 1978; Hsu and  
340 Jeng, 1994; Ye et al., 2014; Tang et al., 2015; Elsafti and Oumeraci, 2016). However, this as-  
341 sumption contradicts to the physical phenomena for waves over a porous seabed. Therefore, the

Table 2: Input data for numerical examples.

Characteristics	Value	Unit
<i>Wave characteristics</i>		
Wave height ( $H$ )	3.0 or various	[m]
Wave period ( $T$ )	8 or various	[s]
Water depth ( $d$ )	10 or various	[m]
Water density ( $\rho_w$ )	1000	[kg/m <sup>3</sup> ]
Bulk modulus of elasticity of water ( $K_w$ )	$2.0 \times 10^9$	[N/m <sup>2</sup> ]
<i>Seabed characteristics</i>		
Permeability ( $k_s$ )	$5 \times 10^{-2}$ or various	[m/s]
Poisson's ratio ( $\mu_s$ )	0.3	–
Porosity ( $n$ )	0.448	–
Degree of saturation ( $S_r$ )	0.98 or various	-
Shear modulus ( $G_s$ )	$5 \times 10^6$ or various	[N/m <sup>2</sup> ]
Density of soil ( $\rho_s$ )	2679	[kg/m <sup>3</sup> ]
Particles size ( $d_{50}$ )	0.8 or various	[mm]
Friction coefficient of soil ( $f$ )	0.58	–
Seabed thickness ( $d_s$ )	30	[m]]

342 two-way coupling model combines seepage velocity and soil displacement induced flow velocity  
 343 as the flow velocity at the interface of fluid and seabed. According to the essential difference  
 344 of the two coupling algorithms, the flow velocity at the interface of fluid and seabed in the  $x$ -  
 345 and  $z$ - direction ( $u_f$  and  $w_f$ ) are plotted in Figure 8. In the figure, the subscript "1" denotes the  
 346 results from one-way coupling model, while "2" is for the results of two-way coupling model.  
 347 It is clear that the maximal flow velocity is about 2 mm/s in the  $x$ - direction and 30 mm/s in  
 348 the  $z$ - direction for the two-way coupling algorithm. Furthermore, the flow velocity in the  $z$ -  
 349 direction is one-magnitude-order larger than flow velocity in the  $x$ - direction, while they are  
 350 zeros with the one-way coupling model. Although the flow velocity at the interface of fluid and  
 351 seabed are small, it will cause the impacts to the flow and seabed characteristics, which will be  
 352 discussed in the following sections.

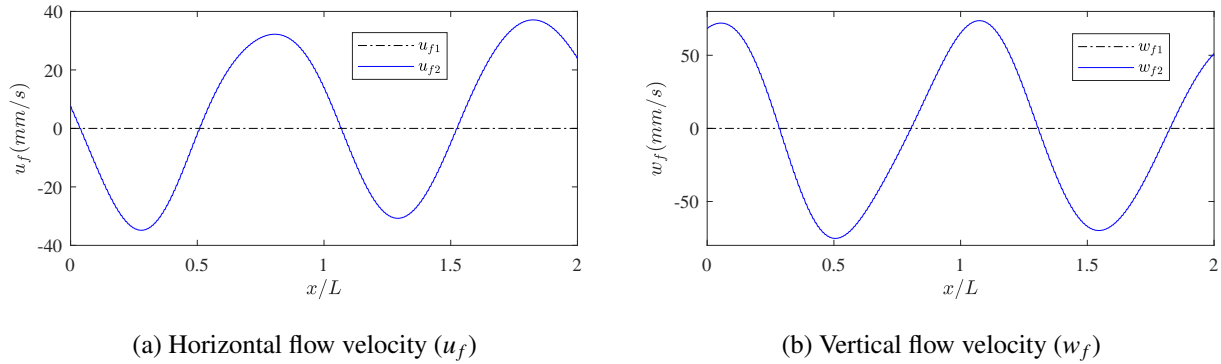


Figure 8: Comparison of flow velocity at the seabed surface ( $z = 0$ ) for different coupling algorithms: (a) variation of horizontal flow velocity at the seabed surface ( $u_f$ ) and (b) variation of vertical flow velocity at the seabed surface ( $w_f$ ). Note: Subscript "1" is the results of one-way coupling model and "2" is for two-way coupling model.

353 The free water surface elevation ( $\eta$ ) is one of important wave parameters in the hydrodynamic  
 354 analysis. The influence of different coupling algorithms on free water surface elevation  
 355 ( $\eta$ ) is illustrated in Figure 9. As shown in the figure, one-way coupling algorithm may slightly  
 356 overestimated the amplitude of wave compared with the results of two-way coupling model.  
 357 However, the difference of water surface elevation caused by one-way coupling and two-way  
 358 coupling algorithm is insignificant in Figure 9(a). To further clarify their difference, we plot  
 359 the the variation of  $\frac{\Delta\eta}{H/2}$  along with time is represented in Figure 9(b), in which  $\Delta\eta (= \eta_2 - \eta_1)$   
 360 represents the difference of the water surface elevation obtained by two-way and one-way coupling  
 361 algorithms. Note that the  $\Delta$  in the following figures have same meaning. As shown in the

362 figure, it is obvious that the range of  $\frac{\Delta\eta}{H/2}$  is about  $\pm 5.212\%$ .

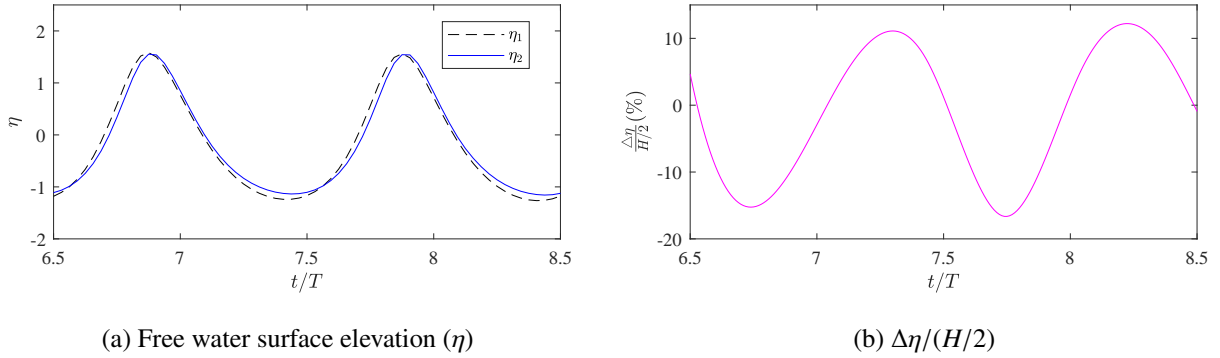


Figure 9: Comparison of free water surface elevation for different coupling algorithms: (a) free water surface elevation ( $\eta$ ) and (b)  $\Delta\eta/(H/2)$ .

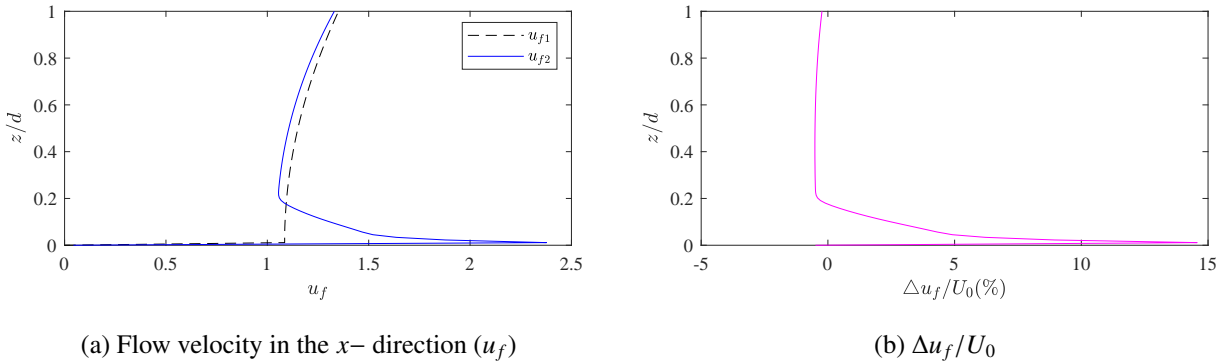


Figure 10: Comparison of flow velocity in the  $x$ - direction for different coupling algorithms: (a) flow velocity ( $u_f$ ) and (b)  $\Delta u_f/U_0$ .

363 In order to further investigate the influence of two coupling algorithms on the fluid fields,  
 364 the distribution of flow velocity in the  $x$ - direction ( $u_f$ ) under the action of wave crest along the  
 365 water depth is represented in Figure 10(a). It is noted in the figure that the flow velocity calcu-  
 366 lated by two-way coupling algorithm has a significant increase near the interface of fluid and  
 367 seabed, which would gradually decrease and then smaller than the results of one-way coupling  
 368 algorithm. Although the flow velocity is too small to be observed at the interface of fluid and  
 369 seabed, as seen from Figure 8(a), it has a great influence on flow velocity in the  $x$ - direction,  
 370 especially near the interface of fluid and seabed. An increased ratio of  $\Delta u_f/U_0$  is introduced to  
 371 reflect the influence level of different coupling algorithms on flow velocity in the  $x$ - direction,  
 372 in which  $U_0(= L/T)$  is the wave velocity. The variation of  $\Delta u_f/U_0$  in the vertical direction is  
 373 illustrated in Figure 10(b). Similar to the change of  $u_f$  along the water depth, the increased ratio

374  $\Delta u_f/U_0$  has a great increase near the interface of fluid and seabed, which could reach about  
 375 815%. Then,  $\Delta u_f/U_0$  quickly reduced to negative values away from the seabed surface, which  
 376 means the flow velocity in the  $x$ - direction by the two-way coupling method would smaller than  
 377 the results of the one-way coupling method away from the seabed surface.

Shields number has been recognised as one of key parameter in the evaluation of sediment motion of scour around hydraulic structures (Chien and Wan, 1998; Sumer and Fredsøe, 2002). The variations of flow velocity at the fluid–seabed interface will directly affect the Shields number ( $\theta$ ), which determine the onset of sediment motion and the process of scour. Figure 11(a) shows the distribution of Shields number at the seabed surface, in which the Shields number is defined by (Shields, 1937):

$$\theta = \frac{\tau_b}{(\gamma_s - \gamma_w) d_{50}} = \frac{\rho_w U_*^2}{(\gamma_s - \gamma_w) d_{50}}, \quad (11)$$

378 where  $\gamma_s$  is the unit weight of the sediment,  $d_{50}$  is the median grain size,  $\tau_b$  is the bed shear  
 379 stress and  $U_*$  is the friction velocity.

In Figure 11(a), the critical Shields number is also included, which can be determined by (Soulsby, 1997):

$$\theta_{cr} = 0.30/(1 + 1.2D^*) + 0.055[1 - e^{-0.02D^*}], \quad D^* = \left[ \frac{g}{\nu^2} \left( \frac{\gamma_s}{\gamma_w} - 1 \right) \right]^{1/3} d_{50} \quad (12)$$

380 where  $D^*$  is the dimensionless diameter of soil particle and  $\nu$  is the kinematic viscosity of water.

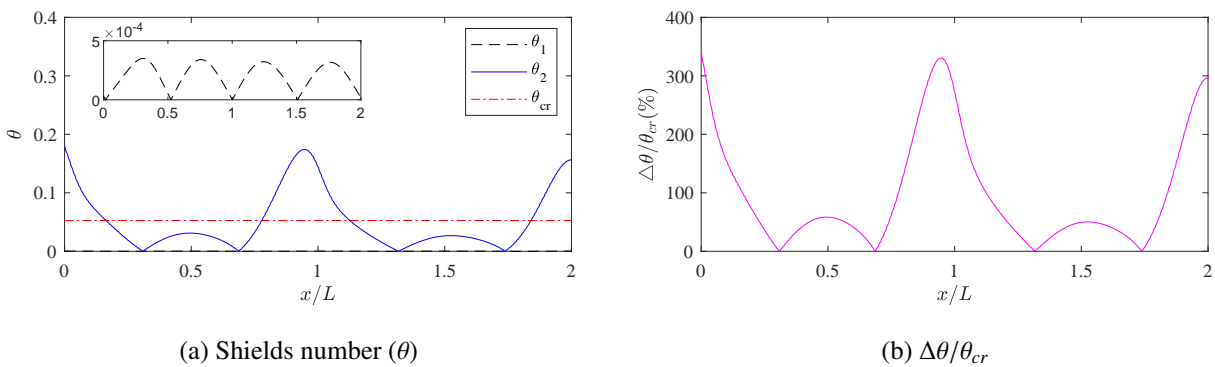


Figure 11: Comparison of Shields number at the interface of fluid and seabed for different coupling algorithms: (a) Shields number ( $\theta$ ) and (b)  $\Delta\theta/\theta_{cr}$ .

381 As shown in Figure 11(a), the Shields number obtained by the one-way coupling algorithm  
 382 is much smaller than that of the two-way coupling algorithm, which has a big difference about

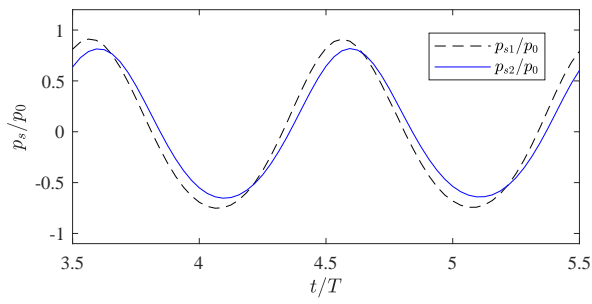
---

383 two or three orders of magnitude. In the case, Shields number obtained from the two-way  
384 coupling algorithm is larger than critical Shields number at the position where the onset of sed-  
385 iment motion occurs. In order to better illustrate the influence of different coupling algorithms  
386 on Shields number, the increased ratio of  $\Delta\theta/\theta_{cr}$  is introduced and the value at the interface of  
387 fluid and seabed is displayed in Figure 11(b). As shown in the figure, the maximal  $\Delta\theta/\theta_{cr}$  can  
388 reach about 150330%, which would further tremendously impact the process of scour. Hence,  
389 the two-way coupling algorithm should be considered for the prediction of sediment motion.

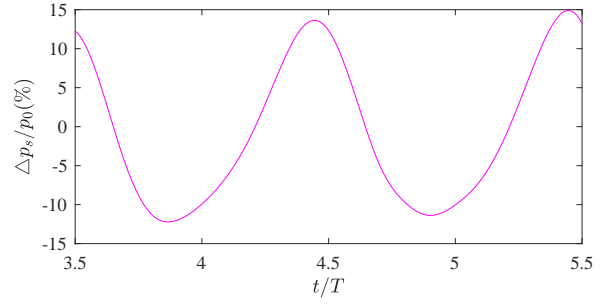
390 In addition to wave characteristics, different coupling algorithms also affect the wave-  
391 induced soil response. Figure 12 presents the influence of different coupling algorithms on  
392 the pore pressures. As shown in Figure 12(a), the amplitude of pore pressure ( $p_s/p_0$ ) at the  
393 seabed surface obtained from the two-way coupling algorithm is smaller than that of the one-  
394 way coupling algorithm. Herein,  $p_0(= \gamma_w H/2 \cosh kd, k$  is wave number) is the amplitude of  
395 linear wave pressures at the seabed surface. Then, the ratio of  $\Delta p_s/p_0$  at the seabed surface  
396 with time is illustrated in Figure 12(b). It is clear that the maximal  $\Delta p_s/p_0$  occurs around wave  
397 crests and troughs, which means the maximal difference of different coupling algorithms on  
398 pore pressure occurs around wave crests and troughs. As seen in the figure, the range of  $\Delta p_s/p_0$   
399 is about  $\pm 6.312\%$ . Meanwhile, the maximum of  $|\Delta p_s/p_0|$  along with seabed depth is presented  
400 in Figure 12(c), which would quickly reduce with the increased seabed depth and then reach a  
401 stable value below one half of seabed depth.

402 The wave-induced soil displacement is another important seabed response parameter. To  
403 investigate the influence of different coupling algorithms on soil displacement, Figure 13(a) de-  
404 picts the absolute maximal soil displacements in the  $x$ - and  $z$ - directions ( $|u_s|$  and  $|w_s|$ ) within  
405 wave cycles, while Figure 13(b) illustrates the relative difference between two models. It is  
406 noted that the absolute maximal soil displacement decreases along seabed depth. However, ab-  
407 solute maximal soil displacement in the  $z$ - direction decrease faster than the value in the  $x$ - direc-  
408 tion. The maximal soil displacement calculated by two-way coupling algorithm is little smaller  
409 than one-way coupling results in both  $x$ - and  $z$ - directions. Furthermore, the increased ratio of  
410  $\Delta u_s/u_{s1}$  would reduce in the  $z$ - direction and hover around a fixed value about -4.516.3% in the  
411  $x$ - direction.

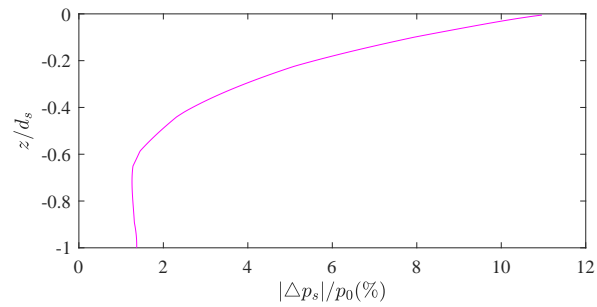
412 The difference of maximal effective normal stresses and shear stress between one-way and



(a)  $p_s/p_0$  at  $z = 0$

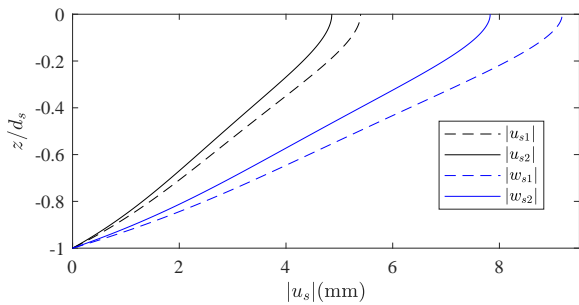


(b)  $\Delta p_s/p_0$  at  $z = 0$

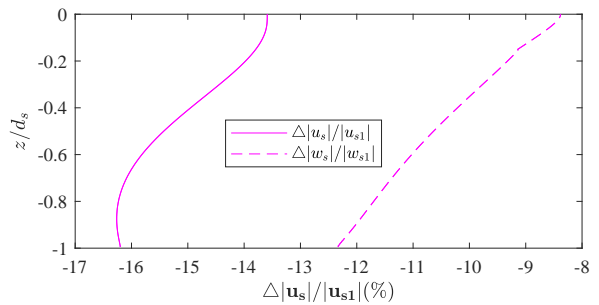


(c)  $|\Delta p_s|/p_0$  vs  $z/d_s$

Figure 12: Comparison of the wave-induced pore-pressures for different coupling algorithms: (a) variation of pore pressure ( $p_s/p_0$ ) at  $z = 0$  vs time, (b) variation of  $\Delta p_s/p_0$  at  $z = 0$  vs time and (c) variation of the maximal  $|\Delta p_s|/p_0$  vs  $z/d_s$ .



(a)  $u_s$  and  $w_s$



(b)  $\Delta \mathbf{u}_s/\mathbf{u}_{s1}$

Figure 13: Comparison of soil displacement along the seabed depth for different coupling algorithms: (a) soil displacement in the  $x$ - and  $z$ - directions ( $u_s$  and  $w_s$ ) and (b)  $\Delta \mathbf{u}_s/\mathbf{u}_{s1}$ .

413 two-way coupling algorithms are analysed and the results are plotted in Figure 14. Among  
414 them, the variation of maximal effective normal stresses in the  $x$ - and  $z$ - directions ( $|\sigma'_{x1}|/p_0$   
415 and  $|\sigma'_{z1}|/p_0$ ) and maximal shear stress ( $|\tau_{xz}|/p_0$ ) along the seabed depth for different coupling  
416 algorithms are illustrated in Figure 14(a)&(c), respectively. It is obvious that the maximal  
417 effective normal stresses in the  $z$ - direction and shear stress increase from zero at the seabed  
418 surface and then decrease in a deeper region. The maximal effective normal stresses in the  $x$ -  
419 direction has the same changed trend but they are not zero at the seabed surface. In general, the  
420 maximal effective normal stresses and shear stress by two-way coupling model are smaller than  
421 that of one-way coupling model. Then,  $\Delta|\sigma'|/p_0$  and  $\Delta|\tau_{xz}|/p_0$  are introduced to explore the  
422 difference of two algorithms on maximal effective normal stresses and shear stress, which are  
423 represented in Figure 14(b)&(d), respectively. As shown in the figures,  $\Delta|\sigma'|/p_0$  and  $\Delta|\tau_{xz}|/p_0$   
424 reduce firstly and then increased with the increased soil depth. The maximal absolute value  
425 of the  $\Delta|\sigma'_{z1}|/p_0$  can reach to about 11.715%, which means the influence of different coupling  
426 algorithms on effective normal stress in the  $z$ - direction is largest compared with other stresses.

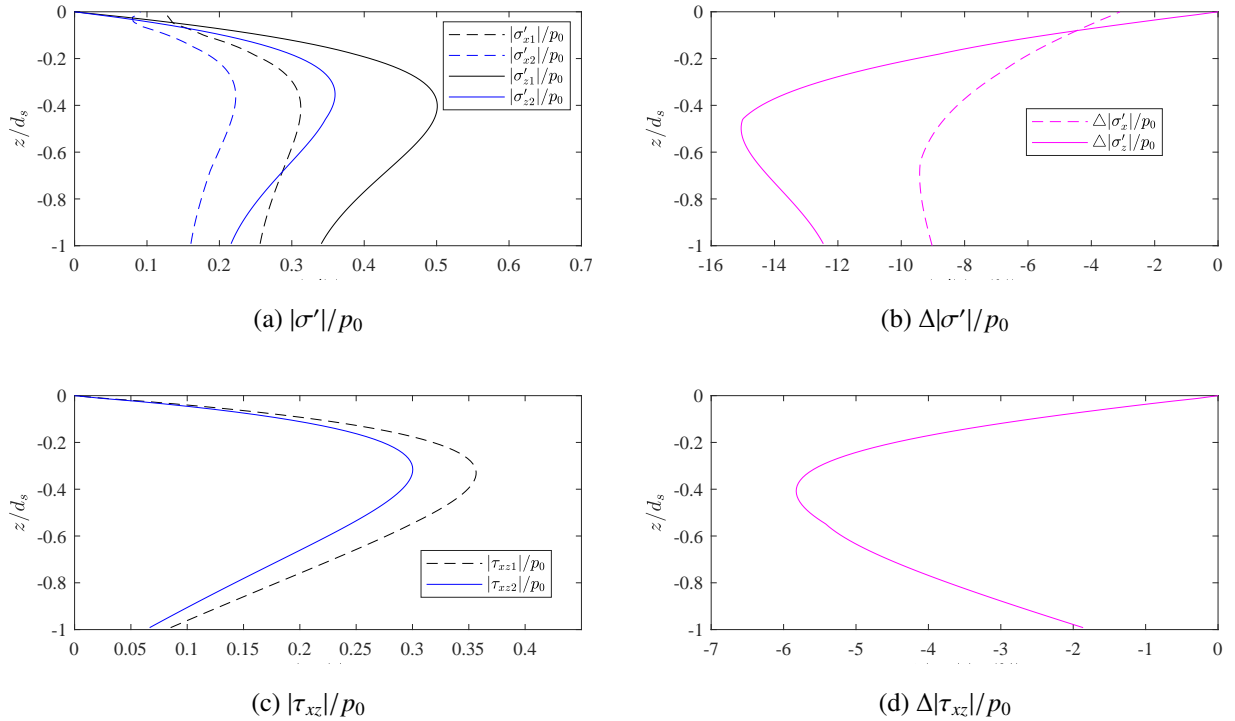


Figure 14: Comparison of the maximal effective normal stresses and shear stress along the seabed depth for different coupling algorithms: (a) maximal effective normal stresses( $|\sigma'|/p_0$ ), (b)  $\Delta|\sigma'|/p_0$ , (c) maximal shear stress ( $|\tau_{xz}|/p_0$ ) and (d)  $\Delta|\tau_{xz}|/p_0$ .

---

## 427 5. Parametric study for wave-seabed interactions in a 2D domain

428 In the last section, the relative differences of wave profile, fluid velocity, Shields number  
429 and soil responses between the one-way and two-way coupling model are discussed under a  
430 specific wave and seabed condition. It is of interesting to further explore the influence of vari-  
431 ous wave (including current) and seabed characteristics on the relative difference between two  
432 approaches.

### 433 5.1. Effects of wave characteristics

434 In the first example, four different wave heights ( $H = 1$  m, 2 m, 3 m and 4 m) are selected  
435 to examine the difference of results between one-way and two-way algorithms and the results  
436 are presented in Figure 15. Herein, four representative increased ratios of  $\Delta u_f/U_0$ ,  $|\Delta p_s|/p_0$ ,  
437  $\Delta|\sigma'_z|/p_0$  and  $\Delta\theta/\theta_{cr}$  are selected for this parametric analysis and the results are plotted in Figure  
438 15. The other parametric analysis also select the same increased ratios and adopt the same  
439 arrangement of results figure, which would not be introduced repeatedly below. It is clear from  
440 Figure 15 that the difference of one-way and two-way coupling algorithms on flow velocity in  
441 the  $x$ - direction, pore-pressure, effective normal stresses in the  $z$ - direction and Shields number  
442 would increase with the wave height generally. As shown in the figure,  $\Delta u_f/U_0$ ,  $|\Delta p_s|/p_0$  and  
443  $\Delta|\sigma'_z|/p_0$  are not more than 2025%. However, the maximal of Shields number could reach to  
444 300650%, which indicates that the Shields numbers at the seabed surface calculated by one-way  
445 and two-way coupling models have great difference with a larger wave.

446 To investigate the influence of water depth ( $d$ ) on wave and seabed characteristics obtained  
447 by one-way and two-way coupling algorithms, four water depths ( $d = 8$  m, 10 m, 15 m and  
448 20 m) are chosen to analyse the influence of water depth. As shown in Figure 16,  $\Delta u_f/U_0$ ,  
449  $|\Delta p_s|/p_0$ ,  $\Delta|\sigma'_z|/p_0$  and  $\Delta\theta/\theta_{cr}$  reduce with the increased water depth overall. This implies that  
450 the difference ~~TWO~~two coupling algorithms will be more significant in shallow water with the  
451 same wave height. Again, more significant impact to  $\Delta\theta/\theta_{cr}$  with the different water depth  
452 is observed in Figure 16(d), which implies the assumption of impermeable interface between  
453 fluid and seabed in one-way coupling model will excessively underestimate the Shields number,  
454 especially in shallow water.

455 In general, the wave period ( $T$ ) will directly affect the wavelength ( $L_0$ ) in conjunction with

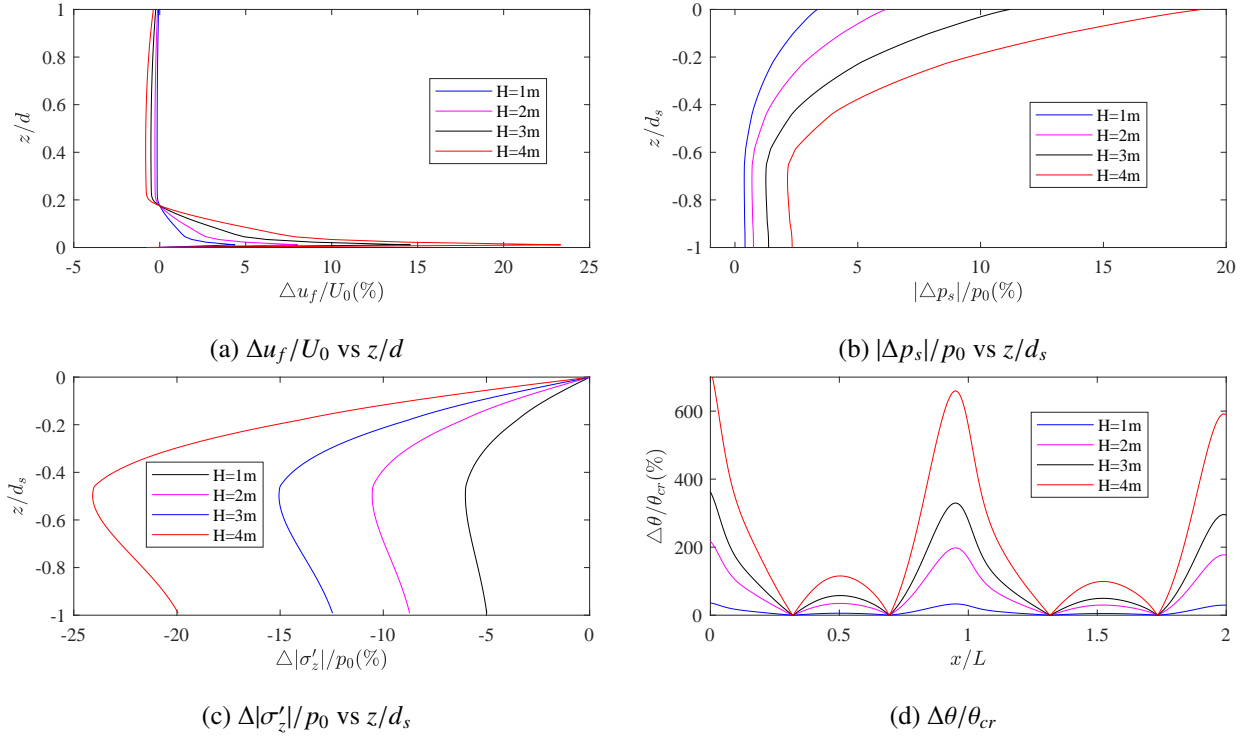


Figure 15: Impact of wave height on flow and seabed field by using different coupling algorithms:(a) $\Delta u_f/U_0$  vs  $z/d$ ; (b)  $|\Delta p_s|/p_0$  vs  $z/d_s$ ; (c)  $\Delta|\sigma'_z|/p_0$  vs  $z/d_s$  and (d)  $\Delta\theta/\theta_{cr}$ .

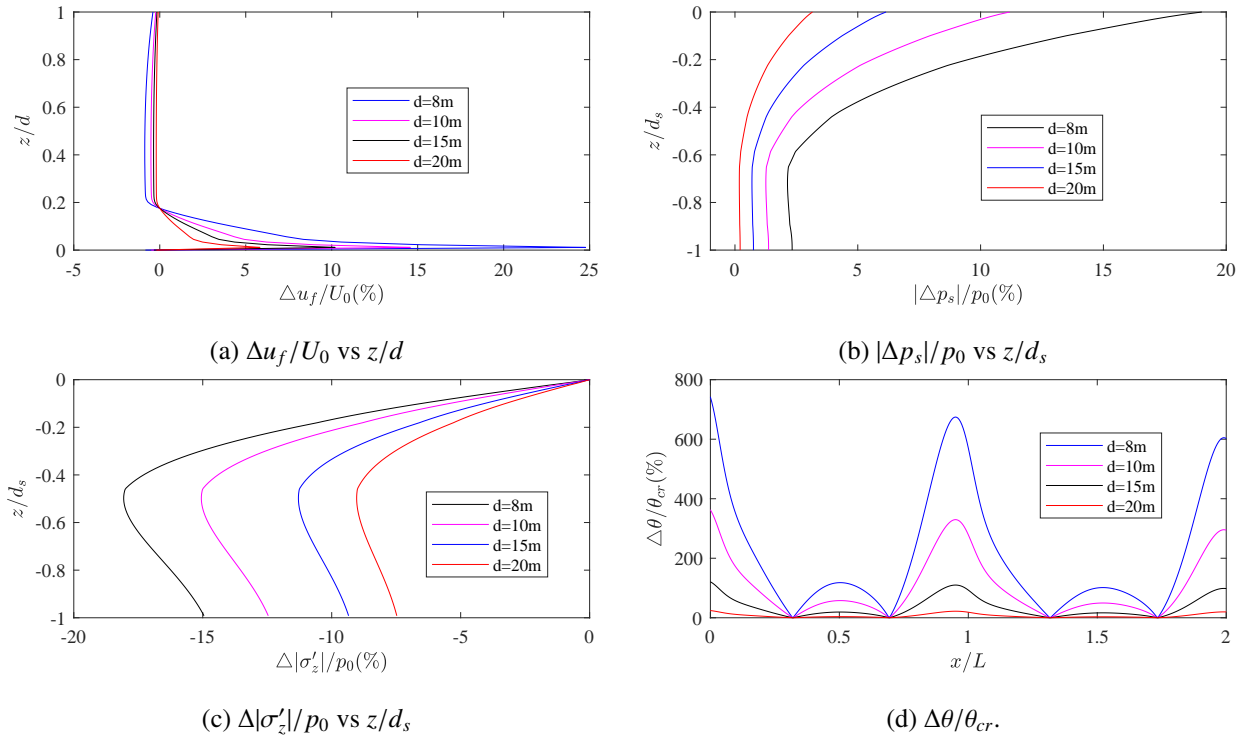


Figure 16: Impact of water depth on flow and seabed field by using different coupling algorithms:(a) $\Delta u_f/U_0$  vs  $z/d$ ; (b)  $|\Delta p_s|/p_0$  vs  $z/d_s$ ; (c)  $\Delta|\sigma'_z|/p_0$  vs  $z/d_s$  and (d)  $\Delta\theta/\theta_{cr}$ .

456 wave height and water depth, which would further impact the wave characteristic of wave field.  
 457 Herein, different wave period ( $T=6s, 8s, 10s$  and  $12s$ ) are selected to investigate the difference of  
 458 flow velocity in the horizontal direction, pore-pressure, effective normal stress in the  $z$ - direction  
 459 and Shields number calculated by two coupling models. Figure 17 illustrates the variations of  
 460 the increased ratios of  $\Delta u_f/U_0$ ,  $|\Delta p_s|/p_0$ ,  $\Delta|\sigma'_z|/p_0$  and  $\Delta\theta/\theta_{cr}$ . As shown in the figure, these  
 461 four increased ratios increase with the wave period. Among them, the influence of wave period  
 462 on  $\Delta|\sigma'_z|/p_0$  not only affects the value but also the shape. Furthermore,  $\Delta|\sigma'_z|/p_0$  would begin to  
 463 decrease earlier with the smaller wave period.

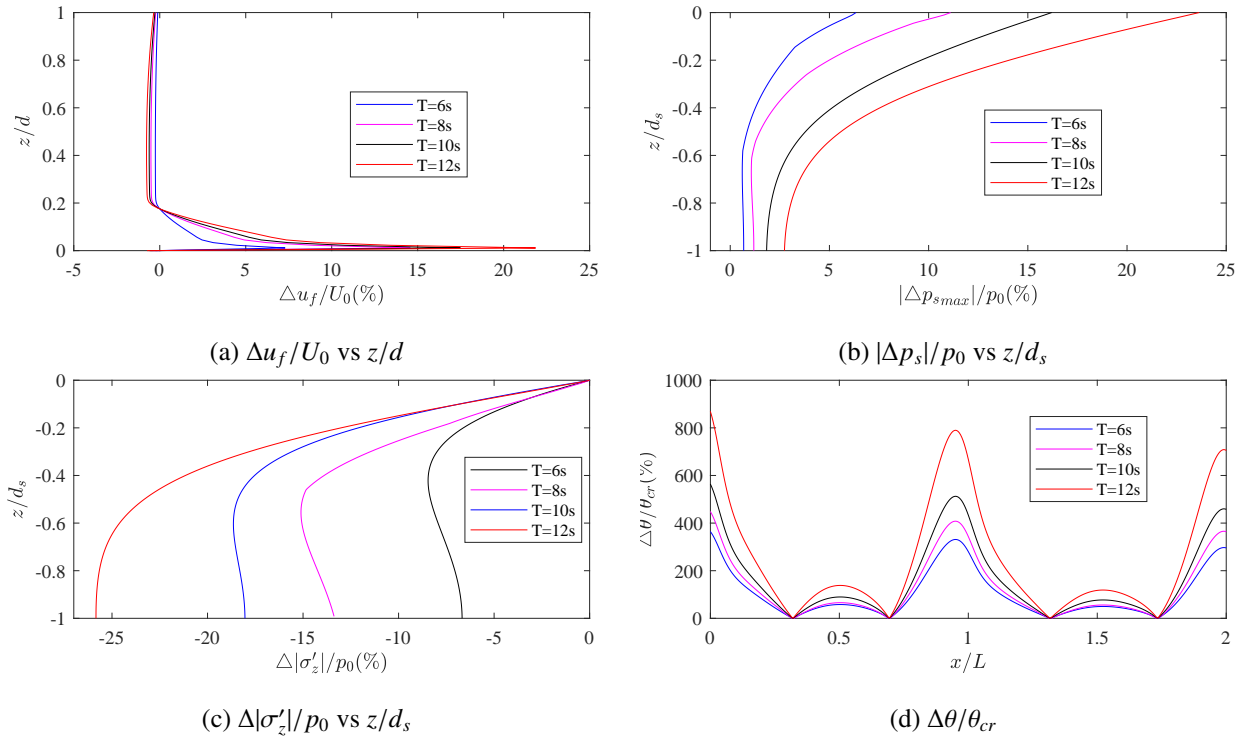


Figure 17: Impact of wave period on flow and seabed field by using different coupling algorithms:(a) $\Delta u_f/U_0$  vs  $z/d$ ; (b)  $|\Delta p_s|/p_0$  vs  $z/d_s$ ; (c)  $\Delta|\sigma'_z|/p_0$  vs  $z/d_s$  and (d)  $\Delta\theta/\theta_{cr}$ .

464 It has been well-known that ocean wave and current coexist to control the hydrodynamic  
 465 behavior in coastal regions. The dynamic seabed response due to combined wave and current  
 466 loading has attracted great attention among coastal engineers (Ye and Jeng, 2012; Wen et al.,  
 467 2012; Liang et al., 2020). Hence, the current velocity is considered as a parameter in the re-  
 468 searching of wave and seabed characteristics obtained by different coupling algorithms. In this  
 469 example, five different current velocities ( $U_c = -0.6 m/s, -0.3 m/s, 0.0 m/s, 0.3 m/s$  and  $0.6$   
 470  $m/s$ ) are chosen to examine the effects of current velocity on fluid and seabed characteristics.

471 In this example, the positive and negative sign of current velocities indicates the the same and  
 472 opposite direction of wave and current, respectively. The variation of the four increased ratios  
 473 of  $\Delta u_f/U_0$ ,  $|\Delta p_s|/p_0$ ,  $\Delta|\sigma'_z|/p_0$  and  $\Delta\theta/\theta_{cr}$  with different current velocities are plotted in  
 474 Figure 18. It is obvious that the existence of current would increase the difference of two cou-  
 475 pling algorithms on flow and seabed characteristics and the difference would increase with the  
 476 increased current velocity. However, the difference of pore-pressures, effective normal stress  
 477 in the  $z$ - direction and Shields number calculated by different coupling models would larger  
 478 with currents traveling along the wave comparing with that currents traveling against the wave.  
 479 Therein, the influence of current  $U_c$  velocity on Shields number is largest, especially for the larger  
 480 flow velocity. On the country, the opposite current velocity would increase the difference of the  
 481 horizontal flow velocity ( $u_f$ ) of one-way and two-way coupling algorithms comparing with the  
 482 results of positive current velocity.

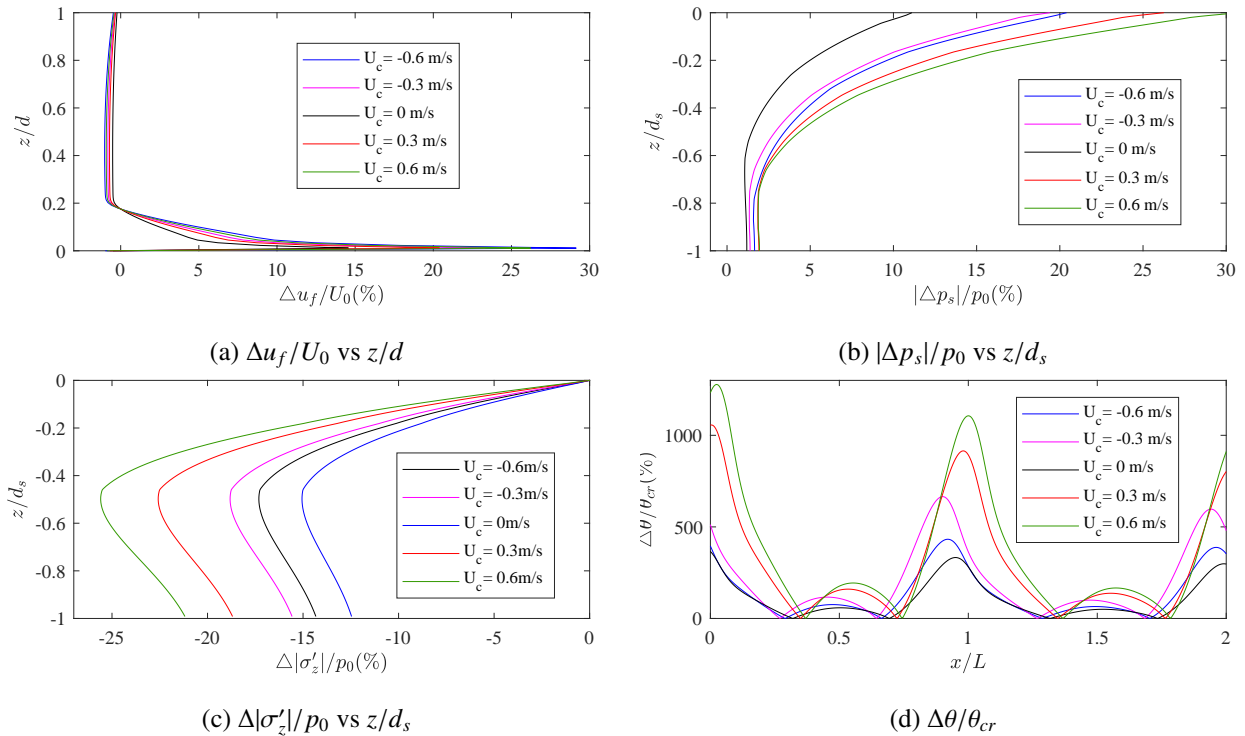


Figure 18: Impact of current velocity ( $U_c$ ) on flow and seabed field by using different coupling algorithms:(a) $\Delta u_f/U_0$  vs  $z/d$ ; (b)  $|\Delta p_s|/p_0$  vs  $z/d_s$ ; (c)  $\Delta|\sigma'_z|/p_0$  vs  $z/d_s$  and (d)  $\Delta\theta/\theta_{cr}$ .

483 In summary, the wave parameters including wave height ( $H$ ), water depth ( $d$ ) and wave pe-  
 484 riod ( $T$ ) and current velocity ( $U_c$ ) all have significant influence on different coupling algorithms,  
 485 especially for the large scale and near breaking waves. However, the current velocity greatly

---

486 affect the Shields number.

## 487 5.2. Effects of seabed characteristics

488 As shown in the governing equations, of (5a)–(5)(5)–(7), numerous soil parameters involved  
489 in the theoretical models. These include the degree of saturation ( $S_r$ ), seabed thickness ( $d_s$ ),  
490 Young modulus ( $G_s$ ), soil permeability ( $k_s$ ), Poisson's ratio ( $\mu_s$ ) and unit weight of soil ( $\gamma_s$ ).  
491 Among these, it has been reported in the literature (Sumer and Fredsøe, 2002; Jeng, 2012), soil  
492 permeability ( $k_s$ ), shear modulus ( $G_s$ ) and degree of saturation ( $S_r$ ) are three parameters that  
493 significantly affect the oscillatory soil response, based on the conventional one-way coupling  
494 models. Therefore, in this section, we conduct a parametric study to examine the effects of  
495 these seabed parameters on the soil response obtained from two different models.

496 In order to explore the influence of soil permeability on fluid and seabed characteristics  
497 obtained by one-way and two-way coupling algorithms, five kind of soil permeability ( $k_s = 5 \times$   
498  $10^{-2}$ ,  $10^{-2}$ ,  $10^{-3}$ ,  $10^{-4}$  and  $10^{-5} m/s$ ) and the corresponding soil particle sizes ( $d_{50} = 8 \times 10^{-4}$ ,  $2 \times$   
499  $10^{-4}$ ,  $1 \times 10^{-4}$ ,  $4 \times 10^{-5}$  and  $2 \times 10^{-5} m$ ) varying from coarse sand to silty sand are selected for the  
500 simulation. The numerical results are plotted in Figure 19. It is clear that the increased ratios  
501 of  $\Delta u_f/U_0$ ,  $|\Delta p_s|/p_0$ ,  $\Delta|\sigma'_z|/p_0$  and  $\Delta\theta/\theta_{cr}$  would increase rapidly with the soil permeability.  
502 And the value of the  $|\Delta p_s|/p_0$ ,  $\Delta|\sigma'_z|/p_0$  are small for permeability less than  $1 \times 10^{-3}$ , which  
503 means the interface of flow and seabed can be regarded as impervious rigid boundary for the  
504 research of soil response and further soil liquefaction for the low permeability seabed. However,  
505  $\frac{\theta_t - \theta_0}{\theta_{cr}}$  should not be ignored although for the low permeability seabed. Therefore, the two-way  
506 coupling algorithm should be adopted for the researching of the sediment incipient motion and  
507 further scour process.

508 We investigate the effects of shear modulus, the following values of shear modulus ( $G_s$   
509  $= 5 \times 10^6$ ,  $1 \times 10^7$ ,  $5 \times 10^7$  and  $1 \times 10^8 Pa$ ) are adopted in the numerical example. As declared  
510 in Figure 20, the increased ratios of  $\Delta u_f/U_0$ ,  $|\Delta p_s|/p_0$ ,  $\Delta|\sigma'_z|/p_0$  and  $\Delta\theta/\theta_{cr}$  would increase as  
511 shear modulus decreases. However, the influences of shear modulus on the four increased ratios  
512 are smaller compared with other parameters such as wave parameters and permeability. This  
513 implies that the shear modulus has little effect on the difference of two coupling results.

514 The degree of saturation has been recognised as one of key parameter for the wave-induced  
515 oscillatory soil response (Jeng, 2018). The influence of saturation degree of soil on wave and

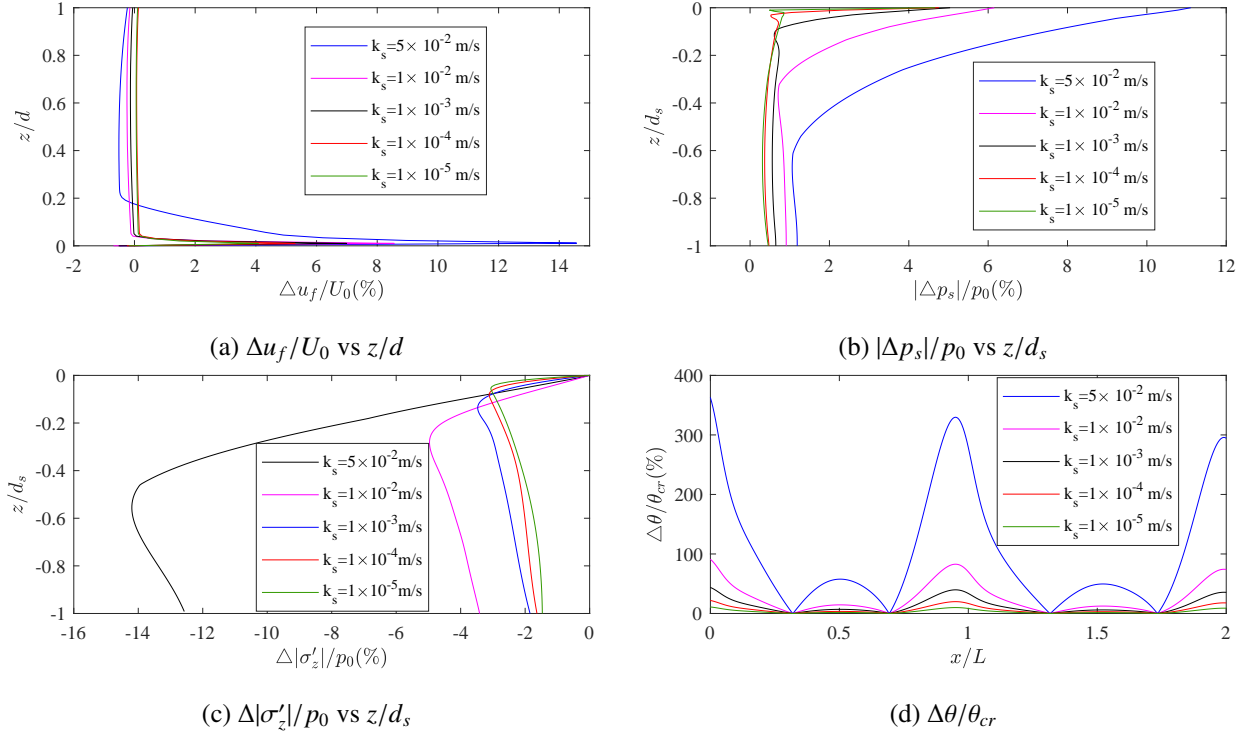


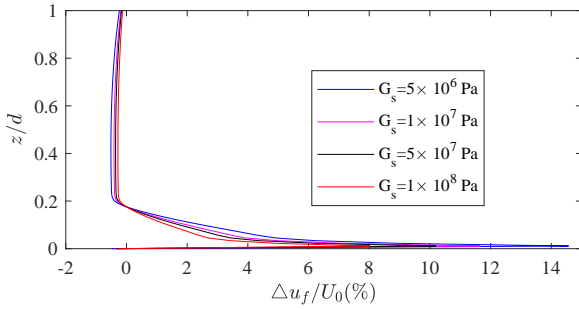
Figure 19: Impact of soil permeability ( $k_s$ ) on flow and seabed field by using different coupling algorithms:(a) $\Delta u_f/U_0$  vs  $z/d_s$ ; (b)  $|\Delta p_s|/p_0$  vs  $z/d_s$ ; (c)  $\Delta|\sigma'_z|/p_0$  vs  $z/d_s$  and (d)  $\Delta\theta/\theta_{cr}$ .

516 seabed characteristic obtained by one-way and two-way coupling models are illustrated in Fig-  
 517 ure 21. Different saturation degrees of soil ( $S_r = 0.95, 0.97, 0.98$  and  $0.99$ ) are selected in the  
 518 example. It is clear that the increased ratios of  $\Delta u_f/U_0$ ,  $|\Delta p_s|/p_0$ ,  $\Delta|\sigma'_z|/p_0$  and  $\Delta\theta/\theta_{cr}$  would  
 519 increase as the degree of saturation increases. Therefore, the saturated soil or near saturated  
 520 soil can ignore the influence of seabed response on flow characteristics. Similar to the shear  
 521 modulus, the influence of saturation degree on the difference of two coupling results is small.

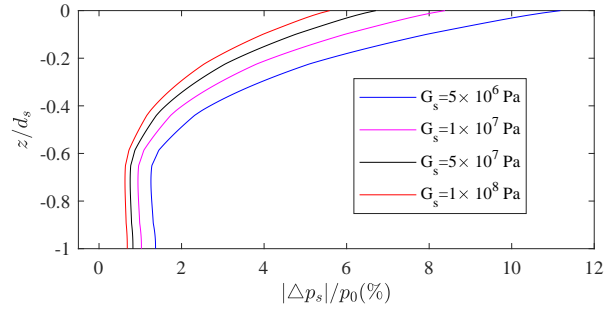
522 In summary, the influence of shear modulus ( $G_s$ ) and degree of saturation ( $S_r$ ) on the dif-  
 523 ference of two coupling algorithms is small. However, soil permeability ( $k_s$ ) significant affects  
 524 the relative difference of two coupling algorithms, particularly the cases with a larger soil per-  
 525 meability ( $k_s$ ) such as  $k_s = 5 \times 10^{-2}$  and  $10^{-2}$ . However, the influence of  $k_s$  can be ignored for  
 526 the permeability less than  $10^{-3}$ .

## 527 6. Engineering applications for 3D problems

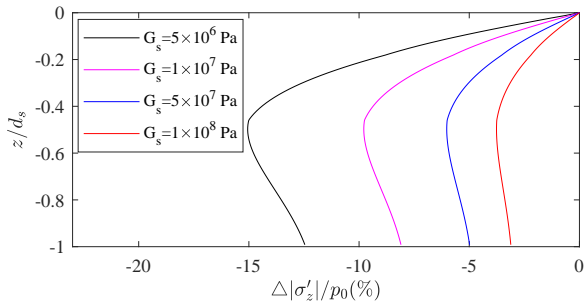
528 In addition to previous sections for the wave-seabed interactions in 2D, we further apply the  
 529 present model to 3D problems. Two typical foundations of mono-pile and dumbbell cofferdam



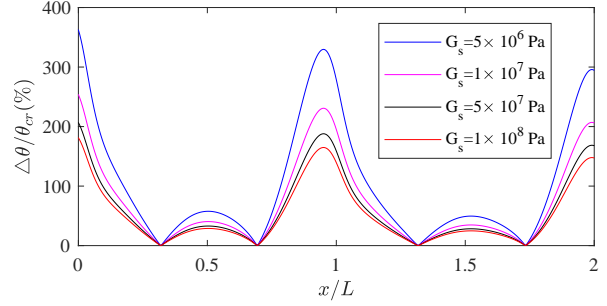
(a)  $\Delta u_f/U_0$  vs  $z/d_s$



(b)  $|\Delta p_s|/p_0$  vs  $z/d_s$

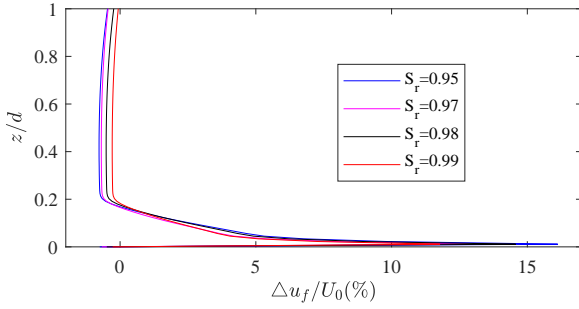


(c)  $\Delta|\sigma'_z|/p_0$  vs  $z/d_s$

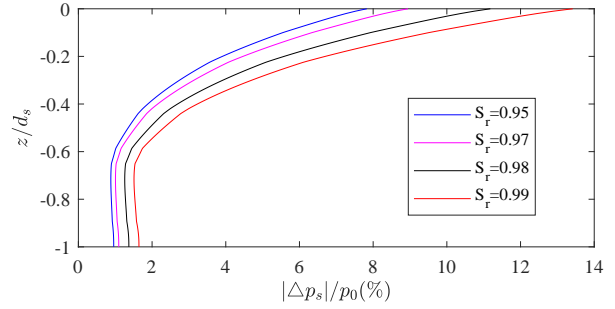


(d)  $\Delta\theta/\theta_{cr}$

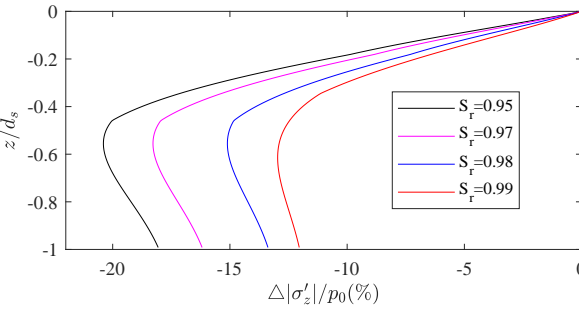
Figure 20: Impact of shear modulus ( $G_s$ ) on flow and seabed field by using different coupling algorithms: (a)  $\Delta u_f/U_0$  vs  $z/d_s$ ; (b)  $|\Delta p_s|/p_0$  vs  $z/d_s$ ; (c)  $\Delta|\sigma'_z|/p_0$  vs  $z/d_s$  and (d)  $\Delta\theta/\theta_{cr}$ .



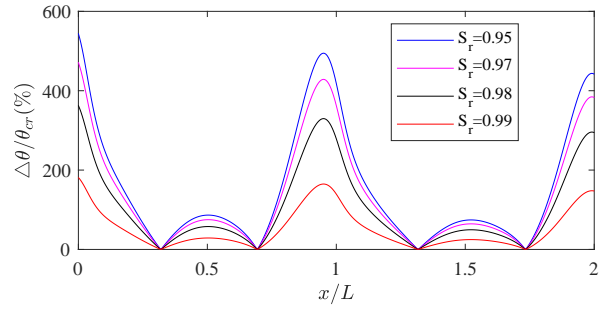
(a)  $\Delta u_f/U_0$  vs  $z/d_s$



(b)  $|\Delta p_s|/p_0$  vs  $z/d_s$



(c)  $\Delta|\sigma'_z|/p_0$  vs  $z/d_s$



(d)  $\Delta\theta/\theta_{cr}$

Figure 21: Impact of degree of saturation ( $S_r$ ) on flow and seabed field by using different coupling algorithms:(a) $\Delta u_f/U_0$  vs  $z/d_s$ ; (b)  $|\Delta p_s|/p_0$  vs  $z/d_s$ ; (c)  $\Delta|\sigma'_z|/p_0$  vs  $z/d_s$  and (d)  $\Delta\theta/\theta_{cr}$ .

530 would be considered to research the influence of different coupling algorithms on wave and  
 531 seabed characteristics around the foundations.

### 532 6.1. 3D case: mono-pile

533 A mono-pile has been commonly used a supporting structures for offshore platforms or  
 534 cross-sea bridges, or offshore wind turbine foundations. Extensive studies have been carried  
 535 out to investigate the seabed response in vicinity of mono-pile in past decades. Li et al. (2011)  
 536 examined the pore pressure around a small diameter pile with linear wave loading. Lin et al.  
 537 (2017) developed a numerical model in OpenFOAM to research the transient soil response  
 538 around a pile with a quasi-static model. Lin et al. (2020) indicated the distributions of the  
 539 effective stress and pore pressure around the pile with currents traveling with the wave.

540 In the section, the problem of fluid-seabed-mono-pile interactions are investigated by the  
 541 proposed two-way coupling model. Figure 22 shows a sketch of the numerical model around  
 542 the mono-pile, which is a classic case for the wave-seabed-pile interactions. As shown in the  
 543 figure,  $L_s$  and  $W_s$  indicate the length and width of the computational domain, respectively. The  
 544 mono-pile is installed in the center of computational domain and the diameter of the mono-  
 545 pile ( $D$ ) is 1 m. In the section,  $L_s$  and  $W_s$  are set to three and two times of the wavelength to  
 546 ignore the influences of the boundary conditions on the flow field around the mono-pile, based  
 547 on previous experience (Ye and Jeng, 2012). The input data of wave and seabed parameters in  
 548 the 3D numerical model are same as the data of 2D model in Table 2.

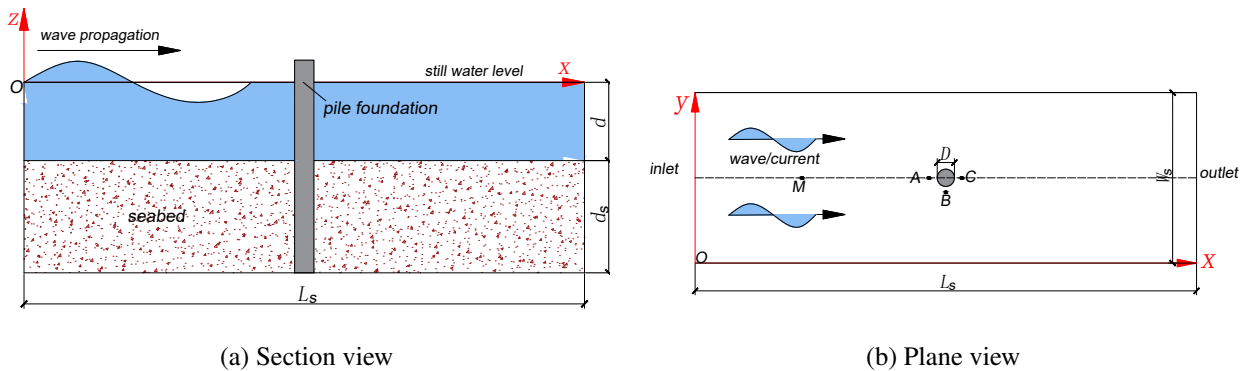


Figure 22: The sketch of the three-dimensional numerical model around the mono-pile.

549 As shown in Figure 23, in a typical wave period ( $t_0 \rightarrow t_0 + 3/4T$ ), the free water surface  
 550 elevation around the mono-pile would have a significant difference. The free water surface

551 elevation would increase in front of the pile and decrease behind the pile, which are due to  
 552 the hindrance before the pile and wake vortex behind the pile for the wave crest. Opposite  
 553 results can be obtained for the wave trough, which is due to the opposite flow direction at wave  
 554 crest and trough. The same phenomenon would occur at other times. The change of free water  
 555 surface elevation around the pile would impact the wave and seabed characteristics. Hence, it is  
 556 necessary to examine the difference of one-way and two-way coupling algorithms on wave and  
 557 seabed characteristics, which are discussed in the following.

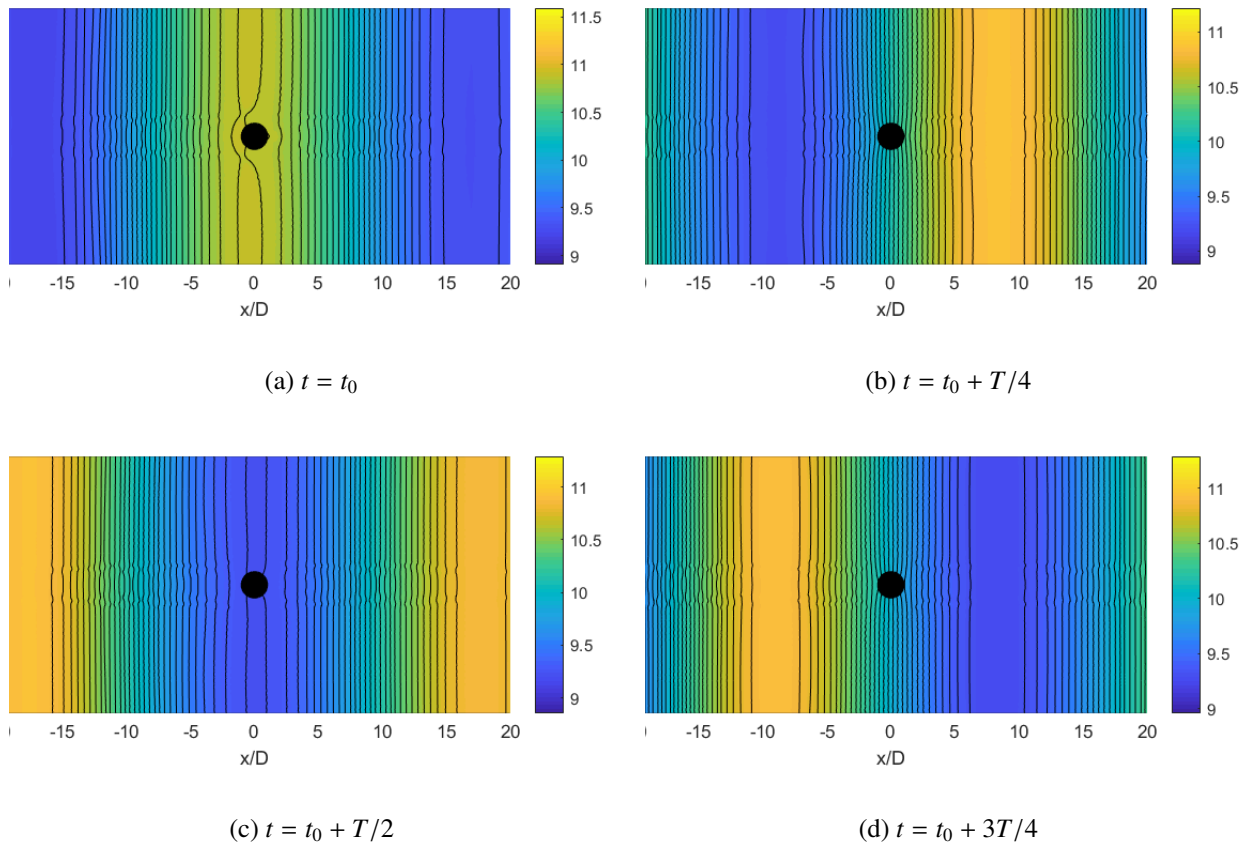


Figure 23: Variations of free water surface elevation around the mono-pile in a wave cycle by two-way coupling algorithm.

558 In Figure 24(a), the flow velocities at the seabed surface around the pile (with  $0.5D$  from  
 559 the pile surface) under wave crests are presented. The angle  $\theta_p$  in the figure is set from  $0^\circ$  to  
 560  $360^\circ$ , as shown in Figure 24(b), which begin from the position in front of the pile and then  
 561 clockwise around the pile to return to original position. The flow velocity in the  $y$ -direction ( $v_f$ )  
 562 at the seabed surface is zero in front of, beside and behind the pile and fluctuate around zero  
 563 at other position, which is due to the roundabout flow phenomenon around the pile. The flow

564 velocity in the  $x$ - and  $z$ - directions ( $u_f$  and  $w_f$ ) are negative and symmetrical with the  $x$ - axis  
 565 in Figure 24(b). However, the minimal and maximal absolute value of flow velocity in the  $x$ -  
 566 direction occurs behind and beside the pile, respectively, which is consistent with the physical  
 567 phenomenon. Meanwhile, the absolute value of flow velocity in the  $z$ - direction is larger than  
 568 the value in the  $x$ - direction and the maximal and minimal absolute value occurs behind and  
 569 beside the pile, which is due to the smaller wave pressure. The minus sign for flow velocity in  
 570 the  $x$ - and  $z$ - direction is due to the co-action of seepage flow and soil displacements.

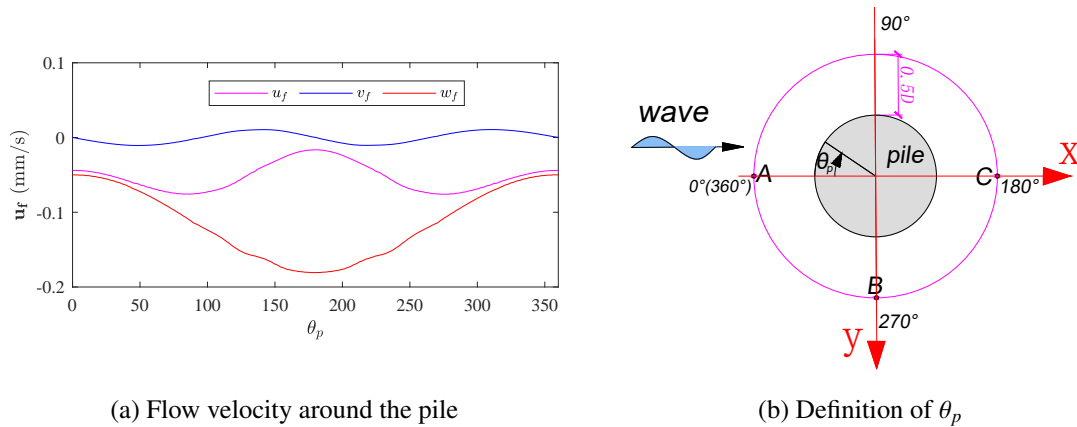


Figure 24: Flow velocity ( $\mathbf{u}_f$ ) (unit:mm/s) around the pile with  $0.5D$  distance from the pile surface at  $z = 0$ .

571 Four positions of M, A, B and C (referring to Figure 22(b)), which are located far away  
 572 the pile for  $1.0L$ , in front of, beside and behind the pile for  $0.5D$ , respectively are selected to  
 573 compare the difference of two coupling algorithms around the pile and the position far away  
 574 from the pile. The variations of water surface elevation with times at the four positions obtained  
 575 by one-way and two-way coupling algorithms are illustrated in Figure 25(a). It is clear that the  
 576 water surface elevation in front of the pile would larger than the results far away the position and  
 577 the water surface elevation behind the pile would smaller than the results far away the position.  
 578 Meanwhile, the amplitude of water surface elevation would be over-estimated if the one-way  
 579 coupling algorithm is adopted, which is same as the results of two-dimensional cases in Figure  
 580 9. In order to investigate the difference of the two coupling algorithms, the comparison of  
 581 increased ratio  $\Delta\eta/(H/2)$  at different positions are illustrated in Figure 25(b). As seen from the  
 582 figure, the  $\Delta\eta/(H/2)$  around the pile is larger than the results far away the pile (i.e., Point M),  
 583 which is due to the changes of flow characteristics in the vicinity of the pile. The maximum  
 584 of  $\Delta\eta/(H/2)$  occurs beside the pile, which is caused by the larger flow velocity beside the pile

585 induced more complex flow characteristics.

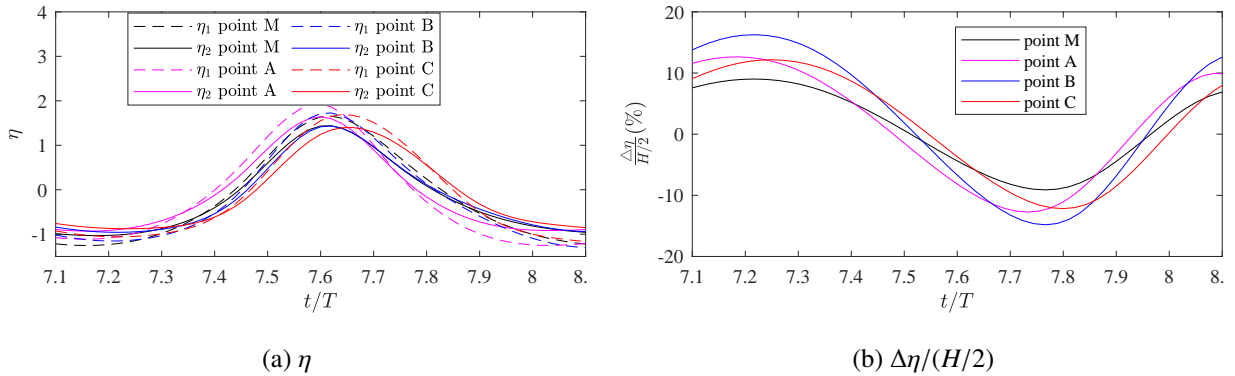


Figure 25: Comparison of free water surface elevation at different positions with different coupling algorithms: (a) variation of free water surface elevation ( $\eta$ ) at different positions and (b) variation of  $\Delta\eta/(H/2)$  at different positions.

586 The comparison of flow velocity under wave crests in the  $x$ - direction along the vertical  
 587 direction at different positions for different coupling algorithms are plotted in Figure 26(a). As  
 588 shown in the figure, the trend of flow velocity in the  $x$ - direction for the case with a pile is similar  
 589 to two-dimensional cases in Figure 10. The flow velocity ( $u_f$ ) is smaller in front of and behind  
 590 the pile, but larger beside the pile, comparing with the results away from the pile. However, it  
 591 is clear the difference of two coupling algorithms is evidently more significant at the positions  
 592 around the pile than the position away from the pile, as shown in Figure 26(b).

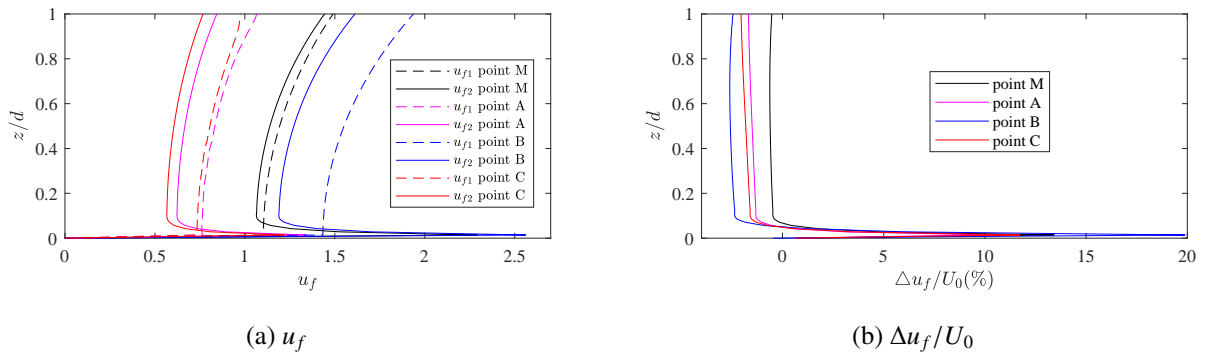


Figure 26: Comparison of horizontal flow velocity direction at different positions with different coupling algorithms: (a) horizontal flow velocity ( $u_f$ ) and (b)  $\Delta u_f/U_0$ .

593 Sediment motion and scour around the pile are important factors endangering the stability  
 594 of the pile-foundation structure in marine environment. Shields number has been recognised  
 595 as one of key parameters in the prediction of scouring and sediment motion around the pile

596 (Sumer and Fredsøe, 2002). The results of Shields number at the locations  $0.5D$  away from  
 597 the pile is plotted in Figure 27(a). Similar to the results of 2D cases, the difference of different  
 598 coupling algorithms on Shields number is extremely large. Furthermore, the maximal Shields  
 599 number occurs beside the pile and the minimum occurs in front of and behind the pile, because  
 600 that the faster flow velocity occurs beside the pile and slower flow velocity occurs before and  
 601 behind the pile due to the hindrance of pile on flow fields. To further demonstrate the difference  
 602 between the one-way and two-way coupling model on Shields number, the increased ratio of  
 603  $\Delta\theta/\theta_{cr}$  around the pile is represented in Figure 27(b). It is obvious that the maximal  $\Delta\theta/\theta_{cr}$   
 604 could reach ~~100~~160%, which indicated that the two-way coupling algorithm is necessary for  
 605 the prediction of the onset of sediment motion.

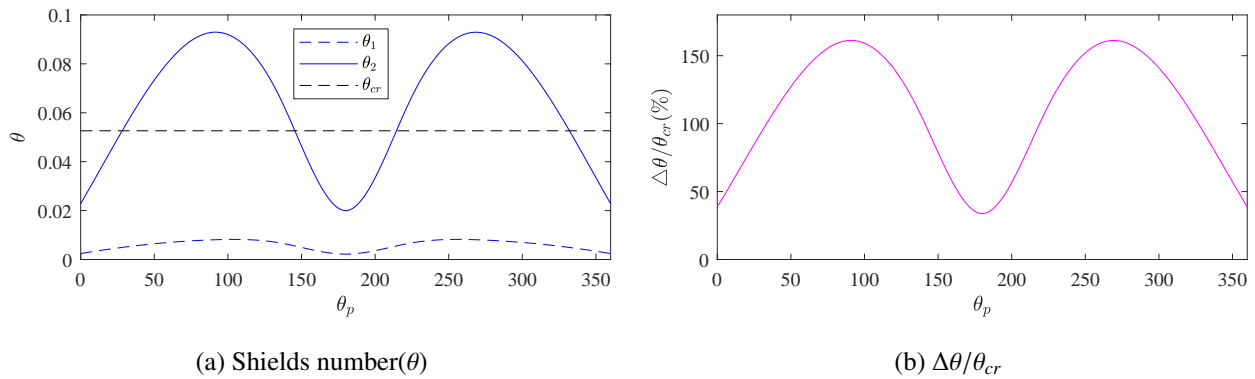


Figure 27: Comparison of Shields number at different positions with different coupling algorithms: (a) Shields number( $\theta$ ) and (b)  $\Delta\theta/\theta_{cr}$ .

606 Wave-induced pore-pressure is a key parameter for the prediction of the seabed liquefac-  
 607 tion, which is one of seabed failure mechanisms to affect the stability of offshore structures.  
 608 Herein, the comparison of pore pressures at the four different positions obtained by two cou-  
 609 pling algorithms in a wave cycle is presented in Figure 28(a). It is clear that the amplitude of  
 610 pore-pressure calculated by two-way coupling model is smaller than that of one-way coupling  
 611 model and the difference of pore-pressure calculated by two coupling models is obvious for the  
 612 positions near the pile. In order to further examine the difference, numerical results of  $\Delta p_s/p_0$   
 613 are plotted in Figure 28(b). It can be seen in the figure that the the maximum of  $\Delta p_s/p_0$  would  
 614 reach to ~~10~~14% around the pile, which is obviously larger than the position far away the pile.  
 615 However,  $\Delta p_s/p_0$  is close at points *A*, *B* and *C* around the pile except for little phase difference.  
 616 The distribution of maximal absolute value of  $|\Delta p_s|/p_0$  along the seabed depth at four different

617 positions is illustrated in Figure 28(c). It is known that the maximal  $|\Delta p_s|/p_0$  for point A is  
 618 obviously smaller than the points around the pile. The  $|\Delta p_s|/p_0$  at point A, B and C around the  
 619 pile is close along the whole seabed depth, but the position in front of the pile is smaller and the  
 620 position behind the pile is larger comparing with the position beside the pile.

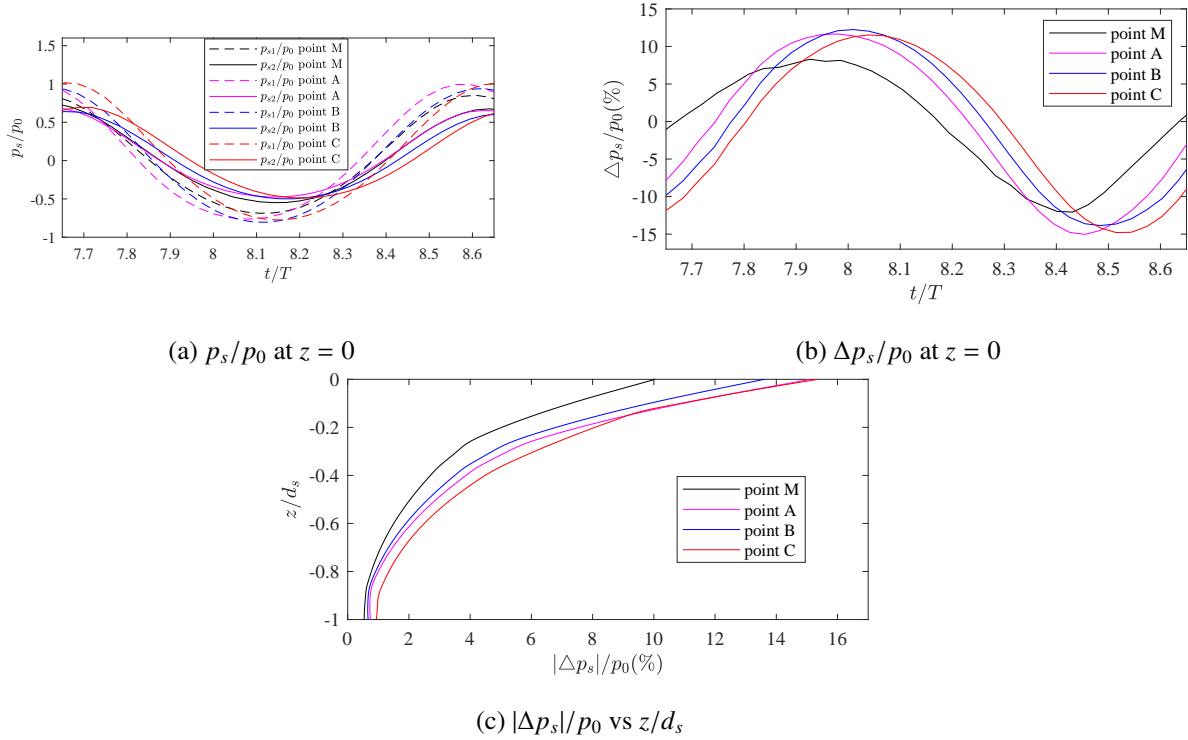


Figure 28: Comparison of wave-induced pore-pressure at different positions with different coupling algorithms: (a) pore pressure ( $p_s/p_0$ ) at  $z = 0$  vs time, (b)  $\Delta p_s/p_0$  at  $z = 0$  vs time and (c) the maximal  $|\Delta p_s|/p_0$  vs  $z/d_s$ .

621 The difference of two coupling models on absolute maximal soil displacements in the  $x$ -,  
 622  $y$ - and  $z$ - directions along the seabed depth ( $z/d_s$ ) at four different positions are represented in  
 623 Figure 29(a), (c) and (e), respectively. It is clear that the soil displacements around the pile are  
 624 always larger than that far away the pile (Point M, referring to Figure 22). That is, the existence  
 625 of a pile would increase the difference between one-way and two-way coupling algorithms  
 626 on soil displacements. Furthermore, the maximum value of soil displacements occurs at the  
 627 position beside the pile. The soil displacements in the  $y$ - direction near zero at Point M, which  
 628 is due to the wave propagation along the  $x$ - direction and has not pressure change in the  $y$ -  
 629 direction. However, the soil displacement in the  $y$ - direction is observed around the pile, which  
 630 is due to the wave diffraction around the pile. The relative difference of soil displacements  
 631 ( $\Delta|\mathbf{u}_s|/|\mathbf{u}_{s1}|$ ) in the  $x$ -,  $y$ - and  $z$ - directions along the seabed depth are plotted in Figure 29(b),

632 (d) and (f), respectively, to more intuitively represent the difference between the two coupling  
 633 methods. The maximal  $\Delta|\mathbf{u}_s|/|\mathbf{u}_{s1}|$  could reach to 928%.

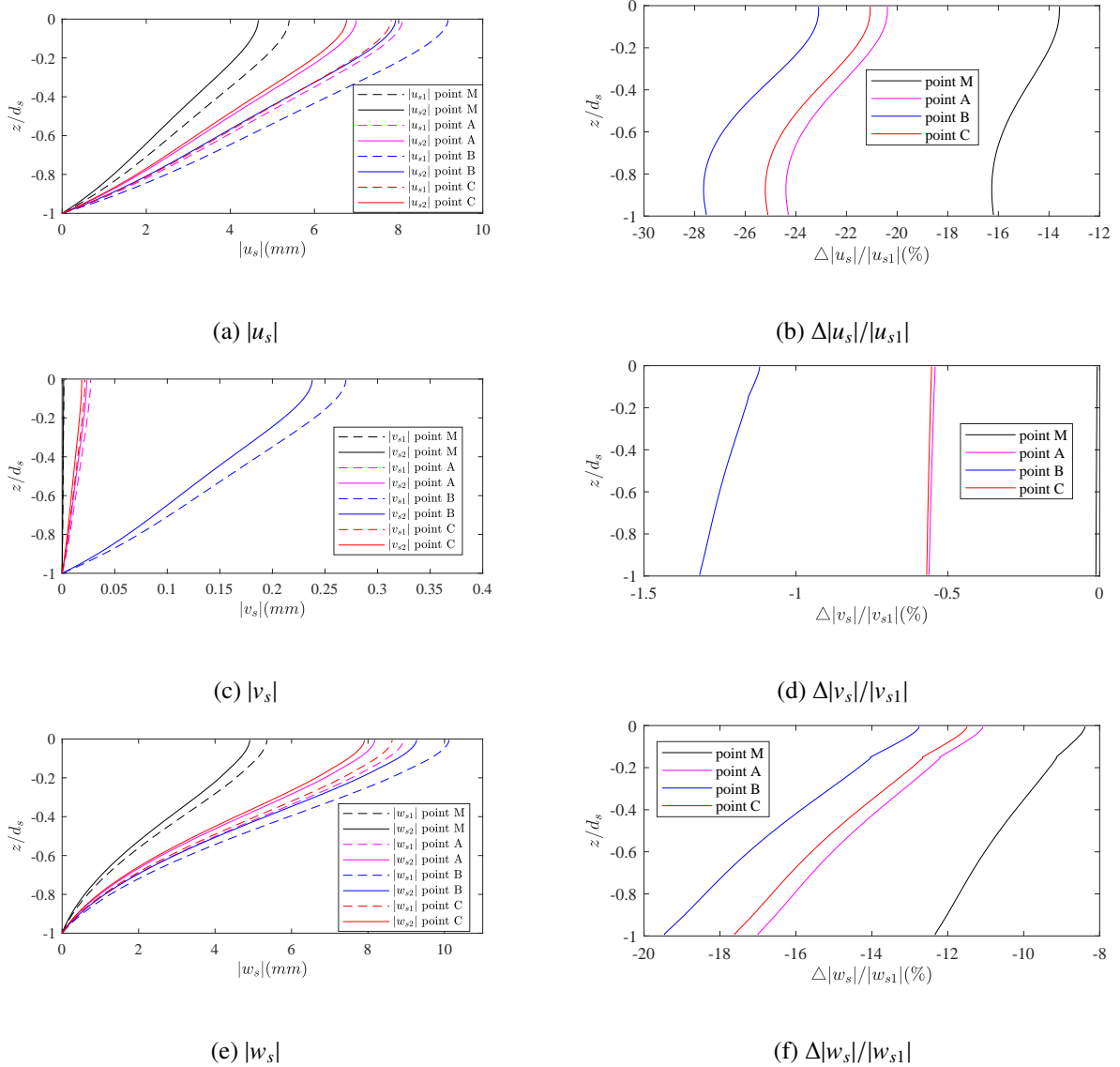


Figure 29: Comparison of maximal soil displacement at different positions with different coupling algorithms: (a) soil displacement in the  $x$ - direction ( $|u_s|$ ), (b)  $\Delta|u_s|/|u_{s1}|$ , (c) soil displacement in the  $y$ - direction ( $|v_s|$ ), (d)  $\Delta|v_s|/|v_{s1}|$ , (e) soil displacement in the  $z$ - direction ( $|w_s|$ ) and (f)  $\Delta|w_s|/|w_{s1}|$ .

634 The difference of effective normal stress obtained by two coupling models at different posi-  
 635 tions are represented in Figure 30. Among them, the variations of effective normal stress in the  
 636  $x$ -,  $y$ - and  $z$ - directions ( $\sigma'_x$ ,  $\sigma'_y$  and  $\sigma'_z$ ) along the soil depth ( $z/d_s$ ) at different positions around  
 637 the mono-pile are illustrated in Figure 30(a), (c) and (e), respectively. It is clear that the effec-  
 638 tive stress around the pile are always larger than the results far away the pile, expect the  $|\sigma'_x|/p_0$

---

639 beside the pile. This means that the existence of pile would increase the difference between  
640 two coupling algorithms on effective normal stress in most cases and the opposite results can  
641 be obtained for the  $|\sigma'_x|/p_0$  beside the pile. Compared the effective normal stress at position *A*,  
642 *B* and *C* around the pile, the maximum value of effective normal stress occurs in front of the  
643 pile and the minimum value occurs beside the pile.

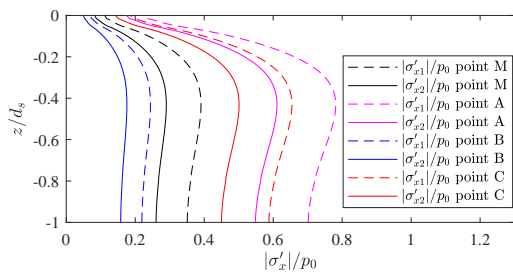
644 In order to explore the influence of different coupling algorithms on effective normal stress  
645 clearly,  $\Delta|\sigma'|/p_0$  in the *x*- *y*- and *z*- directions are introduced and the results of the increased  
646 ratios at different positions are illustrated in Figure 30(b), (d) and (f), respectively. It is obvious  
647 that the difference of two coupling algorithms on effective normal stress around the pile is larger  
648 than the results far away the pile. The maximal  $\Delta|\sigma'|/p_0$  is observed at the effective normal  
649 stress in *z*- direction for the position in front of the pile, which can reach to about 1420%. With  
650 such a difference, the two-way coupling algorithms should be applied for the seabed response  
651 around the pile.

652 Figure 31 illustrates the distribution of shear stresses ( $|\tau_{xy}|/p_0$ ,  $|\tau_{xz}|/p_0$ ,  $|\tau_{yz}|/p_0$ ) and relative  
653 difference between two models ( $\Delta|\tau_{xy}|/p_0$ ,  $\Delta|\tau_{xz}|/p_0$  and  $\Delta|\tau_{yz}|/p_0$ ) versus soil depth ( $z/d_s$ ). The  
654 shear stresses  $\tau_{xy}$ ,  $\tau_{yz}$  and relative difference between two models  $\Delta|\tau_{xy}|/p_0$  and  $\Delta|\tau_{yz}|/p_0$  are  
655 tiny to near zero, although the value at the position beside the pile has the order of magnitude  
656 increase compared with other positions. However,  $|\tau_{xz}|/p_0$  around the pile is obviously smaller  
657 than the position far away the pile and the minimum and maximum occurs behind and beside  
658 the pile, which has the same change trend with  $\Delta|\tau_{xz}|/p_0$ .

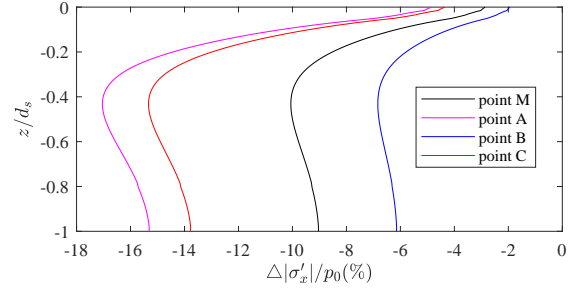
## 659 6.2. 3D case: Dumbbell Cofferdam

660 Cofferdam has been frequently used as a temporal structure during the construction of ma-  
661 rine structures, in which the dumbbell cofferdam is most common form of cofferdams. In this  
662 section, the sketch of wave-seabed-dumbbell cofferdam interactions is given in Figure 32. The  
663 size of computational domain is the same as the 3D case for mono-pile. The dumbbell cof-  
664 ferdam is located in the center of the computational domain and the detailed size is plotted in  
665 Figure 32. Meanwhile, the input data for this case is same as the data of two-dimensional case  
666 in Table 2.

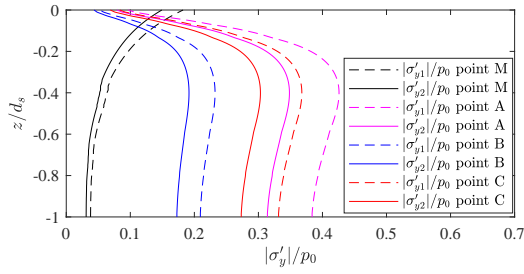
667 To investigate the difference of two coupling algorithms on wave and seabed characteristics  
668 around the dumbbell cofferdam, seven typical positions of *A* – *G* at a distance of 0.5m from the



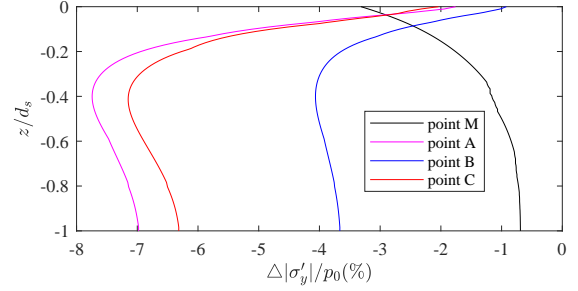
(a)  $|\sigma'_x|/p_0$



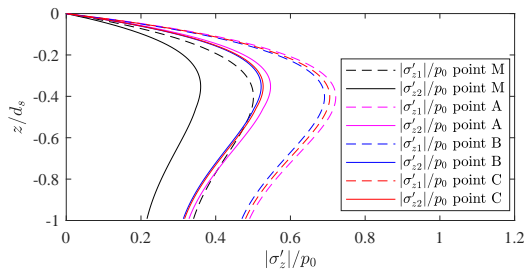
(b)  $\Delta|\sigma'_x|/p_0$



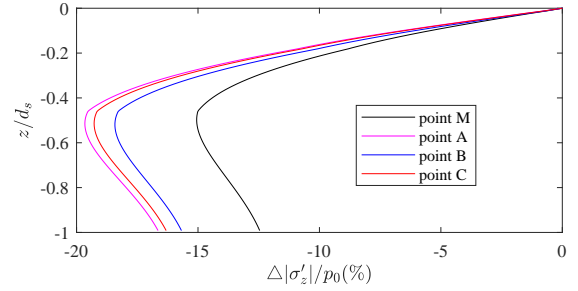
(c)  $|\sigma'_y|/p_0$



(d)  $\Delta|\sigma'_y|/p_0$

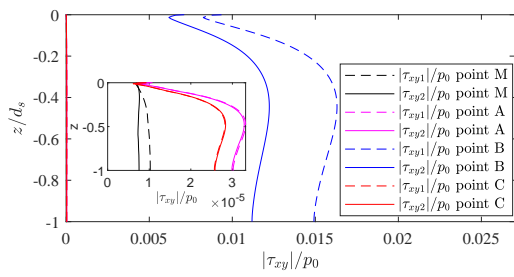


(e)  $|\sigma'_z|/p_0$

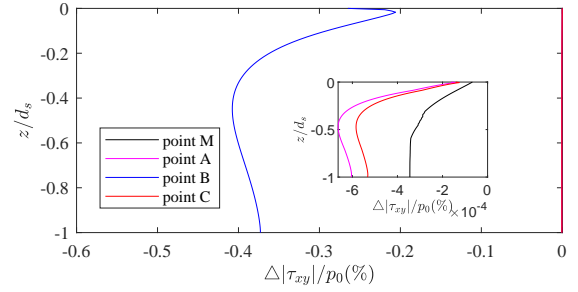


(f)  $\Delta|\sigma'_z|/p_0$

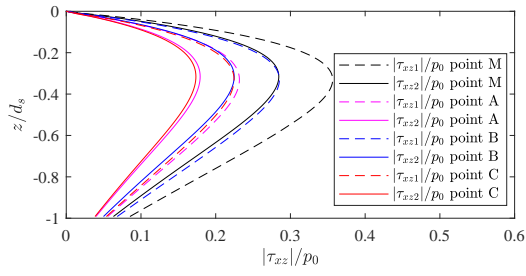
Figure 30: Comparison of effective normal stress at different positive with different algorithms: (a) effective normal stress in the  $x$ - direction( $|\sigma'_x|/p_0$ ), (b)  $\Delta|\sigma'_x|/p_0$ , (c) effective normal stress in the  $y$ - direction( $|\sigma'_y|/p_0$ ),(d)  $\Delta|\sigma'_y|/p_0$ ,(e) effective normal stress in the  $z$ - direction( $|\sigma'_z|/p_0$ ) and (f)  $\Delta|\sigma'_z|/p_0$ .



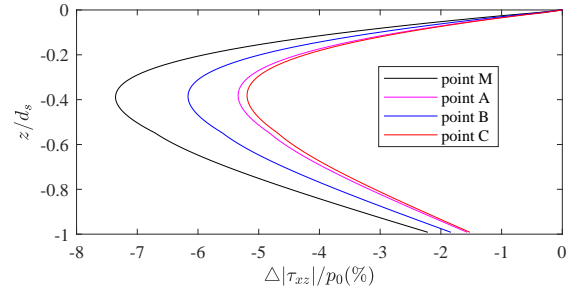
(a)  $|\tau_{xy}|/p_0$



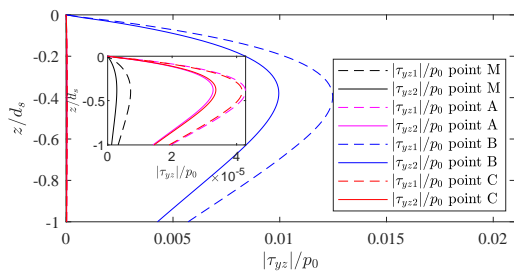
(b)  $\Delta|\tau_{xy}|/p_0$



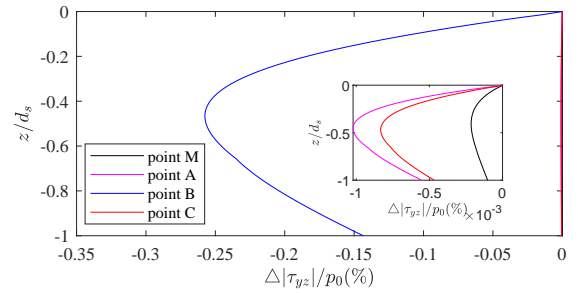
(c)  $|\tau_{xz}|/p_0$



(d)  $\Delta|\tau_{xz}|/p_0$



(e)  $|\tau_{yz}|/p_0$



(f)  $\Delta|\tau_{yz}|/p_0$

Figure 31: Comparison of shear stress at different positive with different algorithms: (a) shear stress in  $xy$ -plane ( $|\tau_{xy}|/p_0$ ), (b)  $\Delta|\tau_{xy}|/p_0$ , (c) shear stress in  $xz$ -plane ( $|\tau_{xz}|/p_0$ ), (d)  $\Delta|\tau_{xz}|/p_0$ , (e) shear stress in  $yz$ -plane ( $|\tau_{yz}|/p_0$ ) and (f)  $\Delta|\tau_{yz}|/p_0$ .

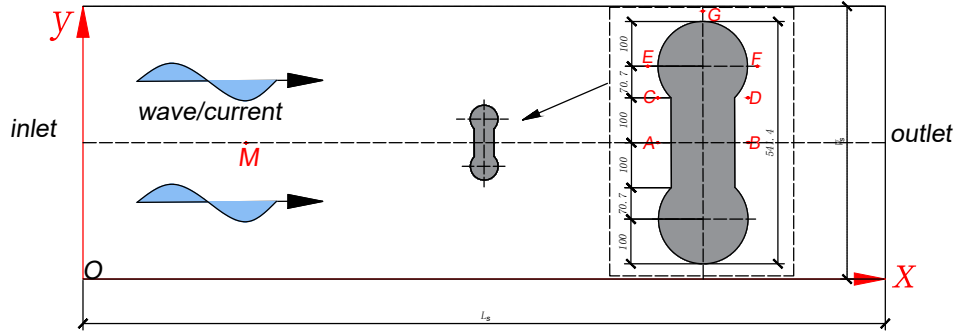


Figure 32: The sketch of the three-dimensional numerical model around the dumbbell cofferdam. (unit:cm)

669 surface of the dumbbell cofferdam and a point of  $M$  before the dumbbell cofferdam for  $1.0L$  are  
 670 selected for the following analysis. Among them, positions  $A$ ,  $C$  and  $E$  are located in front of  
 671 the dumbbell cofferdam and positions  $B$ ,  $D$  and  $F$  are behind it, relative to the wave propagation  
 672 direction; position  $G$  is on the lateral side of the dumbbell cofferdam, as detailed description in  
 673 Figure 32.

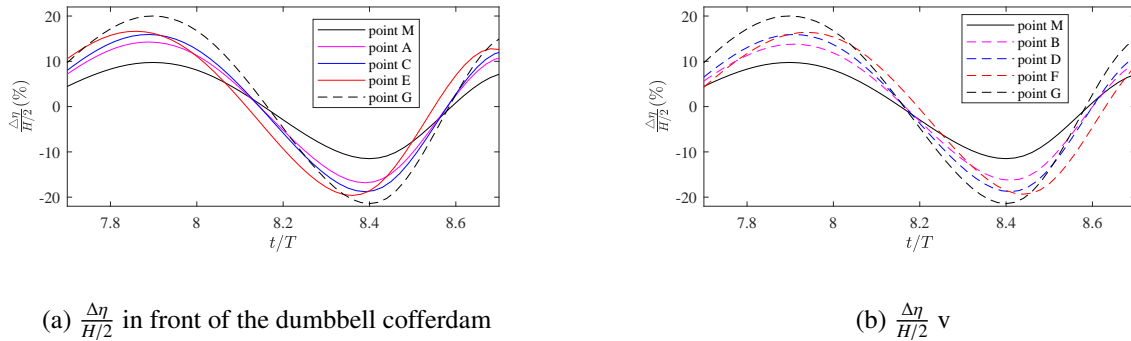


Figure 33: Comparison of free water surface elevation at different positions for different coupling algorithms: (a)  $\Delta\eta/(H/2)$  at positions  $M$ ,  $A$ ,  $C$ ,  $E$  and  $G$  in front of the dumbbell cofferdam and (b)  $\Delta\eta/(H/2)$  at positions  $M$ ,  $B$ ,  $D$ ,  $F$  and  $G$  behind the dumbbell cofferdam.

674 Herein, free water surface elevation and horizontal flow velocity along vertical direction are  
 675 selected to explore the the difference of two coupling algorithms on wave characteristics around  
 676 the dumbbell cofferdam. The variations of  $\frac{\Delta\eta}{H/2}$  and  $\Delta u_f/U_0$  are indicated in Figures 33 and 34,  
 677 respectively. As shown in Figure 33, the phase difference exists due to different  $x$ - coordinate  
 678 value for the different positions around the dumbbell cofferdam. It is noted that  $\frac{\Delta\eta}{H/2}$  and  $\Delta u_f/U_0$

679 around the dumbbell cofferdam are significantly larger than the results far away the dumbbell  
 680 cofferdam. Meanwhile, the amplitude of  $\frac{\Delta\eta}{H/2}$  at the positions in front of the dumbbell cofferdam  
 681 is slightly larger than the results behind the dumbbell cofferdam, The same conclusion can be  
 682 obtained for the horizontal flow velocity ( $\Delta u_f/U_0$ ), as shown in Figure 34.

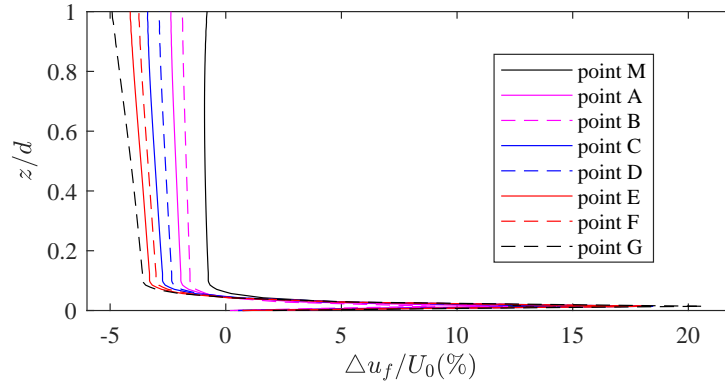


Figure 34: Comparison of the relative difference of flow velocity in the  $x$ - direction ( $\Delta u_f/U_0$ ) between two coupling algorithms at different positions.

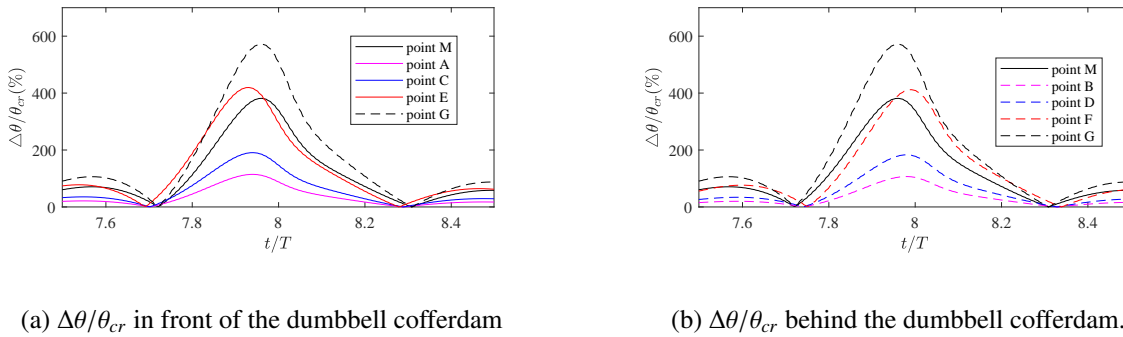


Figure 35: Comparison of Shields number at different positions for different coupling algorithms: (a)  $\Delta\theta/\theta_{cr}$  at positions M, A, C, E and G in front of the dumbbell cofferdam and (b)  $\Delta\theta/\theta_{cr}$  at positions M, B, D, F and G behind the dumbbell cofferdam.

683 As discussed in the previous sections, there is a large difference of two coupling algorithms  
 684 on Shields number, which is important for the stability of structures. To further examine the  
 685 influence of different coupling methods on Shields number around the dumbbell cofferdam, the  
 686 variation of  $\Delta\theta/\theta_{cr}$  in different positions are plotted in Figure 35. As shown in the figure, the  
 687 difference of Shields number between two coupling methods is larger at the positions beside the  
 688 dumbbell cofferdam and smaller at the positions in front of and behind the dumbbell cofferdam,

689 comparing with the point  $M$ , at which the influence of dumbbell cofferdam is ignored because it  
 690 is far from the structure. It can be concluded that  $\Delta\theta/\theta_{cr}$  is so large to illustrate that the one-way  
 691 coupling model is inappropriately to describe the process of scour around the structures.

692 The influence of different coupling algorithms on pore pressures ( $|\Delta p_s|/p_0$ ) around the  
 693 dumbbell cofferdam is presented in Figure 36. It is observed from the figure that  $|\Delta p_s|/p_0$   
 694 increase around the the dumbbell cofferdam compared with the position  $MM$  far away the  
 695 dumbbell cofferdam. Furthermore, the difference of two coupling methods on pore pressures  
 696 is larger at the positions in front of the dumbbell cofferdam comparing with the corresponding  
 697 positions behind the dumbbell cofferdam.

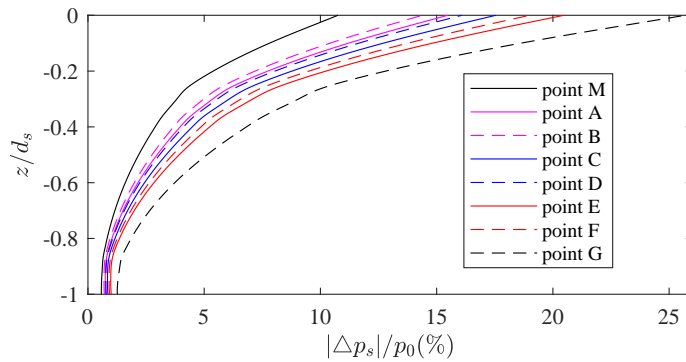


Figure 36: Comparison of pore pressures along the seabed depth at different positions for different coupling algorithms.

698 The difference between two coupling models on soil displacements ( $|\mathbf{u}_s|/|\mathbf{u}_{s1}|$ ) around dumb-  
 699 bell cofferdam are illustrated in Figure 37. As seen from the figure, the soil displacements  
 700 around the dumbbell cofferdam always larger than the position far away the dumbbell coffer-  
 701 dam (Point  $M$ ). That is, the existence of dumbbell cofferdam would increase the difference  
 702 between two coupling algorithms on soil displacements. The maximum value of  $|\mathbf{u}_s|/|\mathbf{u}_{s1}|$  in the  
 703  $x$ - and  $z$ - directions occur at the position  $GG$  beside the pile and in the  $y$ - direction occurs at  
 704 position  $EE$ .

705 Figure 38 illustrates the relative difference of wave induced stresses between two models.  
 706 As shown in the figure,  $\Delta|\sigma'|/p_0$  around the dumbbell cofferdam are larger than the position far  
 707 away the dumbbell cofferdam and the value in front of the dumbbell cofferdam is always larger  
 708 than the corresponding positions behind the dumbbell cofferdam expect the point  $GG$  beside the

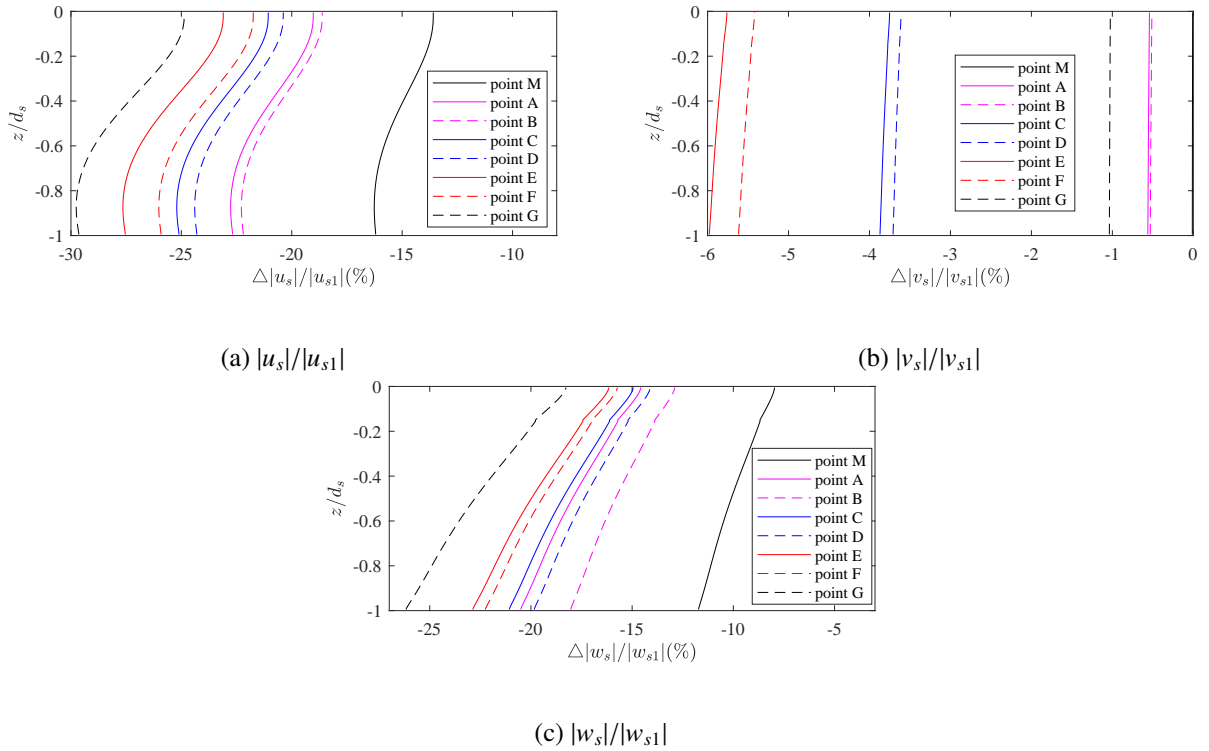
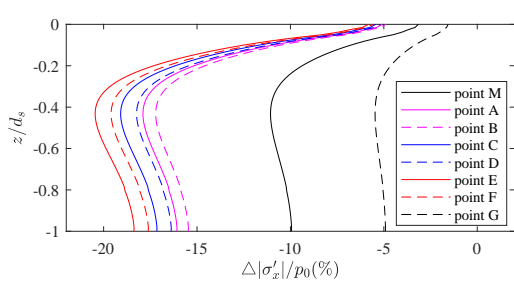


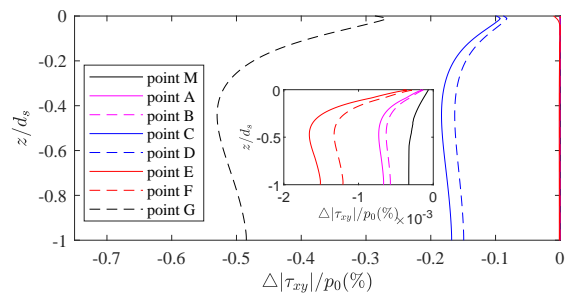
Figure 37: Comparison of soil displacements at different positions with different algorithms: (a)  $|u_s|/|u_{s1}|$ , (b)  $|v_s|/|v_{s1}|$  and (c)  $|w_s|/|w_{s1}|$ .

709 dumbbell cofferdam. However, the difference of shear stress in the  $xy$ - and  $yz$ - plane obtained  
 710 by two coupling algorithms are small that the corresponding increased ratios all less than 0.5%,  
 711 which can be ignored. On the contrary, the existence of dumbbell cofferdam would decrease  
 712 the difference of shear stress in the  $xz$ - plane obtained by different algorithms.

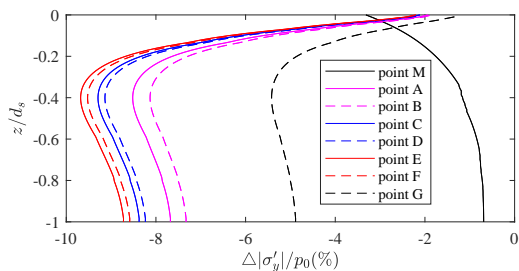
713 In general, the existing a structure will significantly alter the flow field in the vicinity of the  
 714 structure. As discussed in the previous sections, wave height will significantly enhance the dif-  
 715 ference between the two-way coupling model and the conventional one-way coupling models.  
 716 Therefore, the alteration of flow field around a marine structure will consequently enhance the  
 717 impact of the proposed model. Using the case of mono-pile as an example, the water surface  
 718 elevation would increase in front of the structures and decrease behind the pile due to the hin-  
 719 drance of the structures on water such as the mono-pile in Figure 23. The flow velocity beside  
 720 the structures would increase. Therefore, the the difference between two coupling algorithms  
 721 around the structure would larger than that without structures. Based on the detailed analy-  
 722 sis around the mono-pile and dumbbell cofferdam, the influence of the two different coupling



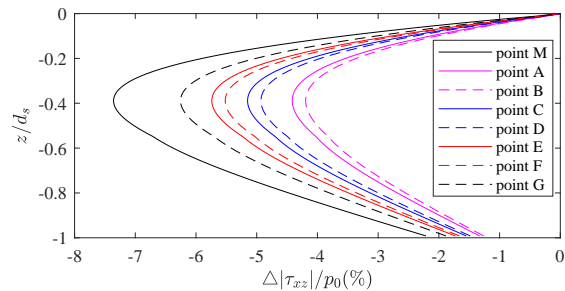
(a)  $\Delta|\sigma'_x|/p_0$



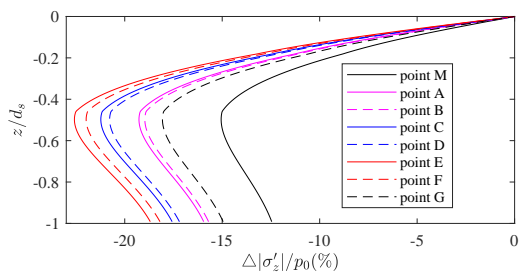
(b)  $\Delta|\tau_{xy}|/p_0$



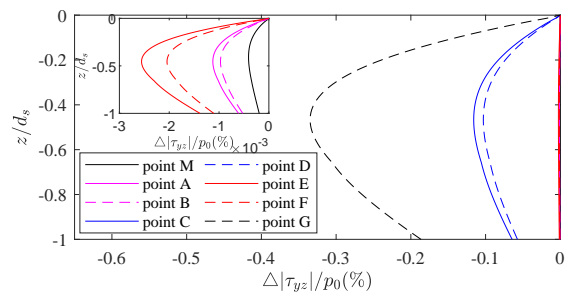
(c)  $\Delta|\sigma'_y|/p_0$



(d)  $\Delta|\tau_{xz}|/p_0$



(e)  $\Delta|\sigma'_z|/p_0$



(f)  $\Delta|\tau_{yz}|/p_0$

Figure 38: Comparison of effective normal stress and shear stress at different positions with different algorithms: (a)  $\Delta|\sigma'_x|/p_0$ , (b)  $\Delta|\tau_{xy}|/p_0$ , (c)  $\Delta|\sigma'_y|/p_0$ , (d)  $\Delta|\tau_{xz}|/p_0$ , (e)  $\Delta|\sigma'_z|/p_0$  and (f)  $\Delta|\tau_{yz}|/p_0$ .

---

723 algorithms on fluid and seabed characteristics is obviously larger than that without structures.  
724 Meanwhile, the larger difference of fluid and seabed characteristics would occurs for larger  
725 structures.

## 726 **7. Conclusions**

727 In this study, the framework of the two-way coupling algorithm is proposed and included  
728 in the existing porous model for WSSI (Liang and Jeng, 2021) in OpenFOAM. With the newly  
729 proposed model, the problem of 2D wave-seabed interactions is considered firstly, and then fur-  
730 ther apply to 3D problem for pile foundation and dumbbell cofferdams. Based on the numerical  
731 results, the following conclusions can be drawn:

- 732 (1) The proposed two-way coupling model assumes the seabed surface is permeable and the  
733 flow velocity caused by seabed response exists at the seabed surface, which was regarded  
734 as impermeable boundary and the flow velocity is zero at the seabed surface for the one-  
735 way coupling model.
- 736 (2) The flow velocity at seabed surface is quite small for the two-way coupling model, which  
737 cause a tremendously increase of the Shields number at the seabed surface and the flow  
738 velocity in the  $x$ - direction near the seabed surface compared with that of one-way cou-  
739 pling model.
- 740 (3) The amplitude of free water surface elevation, pore-pressure , soil displacements , effective  
741 normal stresses and shear stresses obtained by the two-way coupling model would be  
742 smaller than that obtained by the compared with that using one-way coupling model.
- 743 (4) Parametric analysis illustrates that larger wave height, current velocity, soil permeability  
744 and smaller water depth, shear modulus, saturation degree would increase the difference  
745 of two coupling model for wave and seabed characteristics, in which the influence of soil  
746 permeability is greatest.
- 747 (5) The existence of structures like mono-pile and dumbbell cofferdam would obviously in-  
748 crease the difference between the two coupling models on wave and seabed characteristics  
749 around them.

---

750 In the study, the pile is set as a rigid pile and the rocking of the mono-pile is not considered  
751 in this study. Hence, the data is not exchange between the seabed and the pile. Therefore, the  
752 problem of fully soil-structure interactions was not considered in the present model. Regarding  
753 the problem of the fully soil-structure interactions is the next phase of our future study.

## 754 **References**

- 755 Alcérreca-Huerta, J.C., Oumeraci, H., 2018. Soil stability analysis for wave-induced mo-  
756 mentary liquefaction beneath porous bonded revetments. *Coastal Engineering* 138, 22–35.  
757 doi:<https://doi.org/10.1016/j.coastaleng.2018.04.003>.
- 758 Biot, M.A., 1941. General theory of three-dimensional consolidation. *Journal of Applied*  
759 *Physics* 26, 155–164. doi:<https://doi.org/10.1063/1.1712886>.
- 760 Biot, M.A., 1956a. Theory of propagation of elastic waves in a fluid-saturated porous solid,  
761 part I: Low frequency range. *The Journal of the Acoustic Society of America* 28, 168–177.  
762 doi:<https://doi.org/10.1121/1.1908239>.
- 763 Biot, M.A., 1956b. Theory of propagation of elastic waves in a fluid-saturated porous solid,  
764 part ii: High frequency range. *The Journal of Acoustic Society of America* 28, 179–191.  
765 doi:<https://doi.org/10.1121/1.1908241>.
- 766 Cha, M., Cho, G.C., 2007. Shear strength estimation of sandy soils using shear wave velocity.  
767 *Geotechnical Testing Journal* 30, 484–495.
- 768 Chien, N., Wan, Z., 1998. *Mechanics of Sediment Transport*. ASCE Press, Virginia.
- 769 Cui, L., Jeng, D.S., 2021. Seabed liquefaction around breakwater heads at a river mouth:  
770 An integrated 3d model. *Ocean Engineering* 242, 110036. doi:[https://doi.org/10.](https://doi.org/10.1016/j.oceaneng.2021.110036)  
771 [1016/j.oceaneng.2021.110036](https://doi.org/10.1016/j.oceaneng.2021.110036).
- 772 Cui, L., Jeng, D.S., Liu, J.W., 2021. Seabed foundation stability around offshore detached  
773 breakwaters. *Applied Ocean Research* 111, 102672. doi:[https://doi.org/10.1016/](https://doi.org/10.1016/j.apor.2021.102672)  
774 [j.apor.2021.102672](https://doi.org/10.1016/j.apor.2021.102672).

---

775 Dean, R., Dalrymple, R.A., 1984. Water wave mechanics for engineers and scientists. World  
776 Scientific. doi:[10.1142/1232](https://doi.org/10.1142/1232).

777 Diaz-Carrasco, P., Croquer, S., Tamimi, V., Lacey, J., Poncet, S., 2021. Advances in numerical  
778 reynolds-average navier-stokes modelling of wave–structure–seabed interactions and scour.  
779 Journal of Marine Science and Engineering 9, 9060611. doi:[https://doi.org/10.  
780 3390/jmse9060611](https://doi.org/10.3390/jmse9060611).

781 Elsafti, H., Oumeraci, H., 2016. A numerical hydro-geotechnical model for marine gravity  
782 structures. Computers and Geotechnics 79, 105–129. doi:[10.1016/j.compgeo.2016.  
783 05.025](https://doi.org/10.1016/j.compgeo.2016.05.025).

784 Elsafti, H., Oumeraci, H., 2017. Analysis and classification of stepwise failure of monolithic  
785 breakwaters. Coastal Engineering 121, 221–239. doi:[https://doi.org/10.1016/j.  
786 coastaleng.2017.01.001](https://doi.org/10.1016/j.coastaleng.2017.01.001).

787 Gatmiri, B., 1992. Response of cross-anisotropic seabed to ocean waves. Journal of Geotech-  
788 nical Engineering, ASCE 118, 1295–1314. doi:[https://doi.org/10.1061/\(ASCE\)  
789 0733-9410\(1992\)118:9\(1295\)](https://doi.org/10.1061/(ASCE)0733-9410(1992)118:9(1295)).

790 Higuera, P., Lara, J.L., Losada, I.J., 2013. Realistic wave generation and active wave absorp-  
791 tion for navier-stokes models: Application to openfoam. Coastal Engineering 71, 102–118.  
792 doi:<https://doi.org/10.1016/j.coastaleng.2012.07.002>.

793 Hirt, C.W., Nichols, B.D., 1981. Volume of fluid (VOF) method for the dynamics of free  
794 boundaries. Journal of Computational Physics 39, 201–225. doi:[https://doi.org/  
795 10.1016/0021-9991\(81\)90145-5](https://doi.org/10.1016/0021-9991(81)90145-5).

796 Hsu, J.R.C., Jeng, D.S., 1994. Wave-induced soil response in an unsaturated anisotropic seabed  
797 of finite thickness. International Journal for Numerical and Analytical Methods in Geome-  
798 chanics 18, 785–807. doi:[10.1002/nag.1610181104](https://doi.org/10.1002/nag.1610181104).

799 Hsu, J.R.C., Jeng, D.S., Lee, C.P., 1995. Oscillatory soil response and liquefaction in an un-  
800 saturated layered seabed. International Journal for Numerical and Analytical Methods in  
801 Geomechanics 19, 825–849. doi:[10.1002/nag.1610191202](https://doi.org/10.1002/nag.1610191202).

- 
- 802 Hsu, J.R.C., Jeng, D.S., Tsai, C.P., 1993. Short-crested wave-induced soil response in a porous  
803 seabed of infinite thickness. *International Journal for Numerical and Analytical Methods in*  
804 *Geomechanics* 17, 553–576. doi:[10.1002/nag.1610170803](https://doi.org/10.1002/nag.1610170803).
- 805 Jeng, D.S., 1997. Soil response in cross-anisotropic seabed due to standing waves. *Jour-*  
806 *nal of Geotechnical and Geoenvironmental Engineering, ASCE* 123, 9–19. doi:[10.1061/  
807  \[\\(ASCE\\) 1090-0241 \\(1997\\) 123:1 \\(9.\]\(https://doi.org/10.1061/\(ASCE\)1090-0241\(1997\)123:1\(9\)](https://doi.org/10.1061/(ASCE)1090-0241(1997)123:1(9)
- 808 Jeng, D.S., 2000. On calculating the length of a short-crested wave over a porous seabed.  
809 *Applied ocean research* 22, 63–73. doi:[10.1016/S0141-1187\(00\)00006-7](https://doi.org/10.1016/S0141-1187(00)00006-7).
- 810 Jeng, D.S., 2012. *Porous models for wave-seabed interaction*. Springer. doi:[10.1007/  
811 \[978-3-642-33593-8\]\(https://doi.org/10.1007/978-3-642-33593-8\).](https://doi.org/10.1007/978-3-642-33593-8)
- 812 Jeng, D.S., 2018. *Mechanics of wave-seabed-structure interactions: modelling, processes and*  
813 *applications*. Cambridge University Press. doi:[10.1017/9781316672266](https://doi.org/10.1017/9781316672266).
- 814 Jeng, D.S., Cha, D., 2003. Effects of dynamic soil behavior and wave non-linearity on the  
815 wave-induced pore pressure and effective stresses in porous seabed. *Ocean Engineering* 30,  
816 2065–2089. doi:[10.1016/S0029-8018\(03\)00070-2](https://doi.org/10.1016/S0029-8018(03)00070-2).
- 817 Jeng, D.S., Hsu, J., 1996. Wave-induced soil response in a nearly saturated sea-bed of finite  
818 thickness. *Géotechnique* 46, 427–440. doi:[10.1680/geot.1996.46.3.427](https://doi.org/10.1680/geot.1996.46.3.427).
- 819 Jeng, D.S., Lin, Y.S., 1996. Finite element modelling for water waves-soil interaction. *Soil*  
820 *Dynamics and Earthquake Engineering* 15, 283–300. doi:[10.1016/0267-7261\(96\)  
821 \[00009-7\]\(https://doi.org/10.1016/0267-7261\(96\)00009-7\).](https://doi.org/10.1016/0267-7261(96)00009-7)
- 822 Jeng, D.S., Rahman, M., 2000. Effective stresses in a porous seabed of finite thickness: Inertia  
823 effects. *Canadian Geotechnical Journal* 37, 1383–1392. doi:[10.1139/cgj-37-6-1383](https://doi.org/10.1139/cgj-37-6-1383).
- 824 Jeng, D.S., Seymour, B.R., 1997. Response in seabed of finite depth with variable permeability.  
825 *Journal of Geotechnical and Geoenvironmental Engineering, ASCE* 123, 902–911. doi:[10.  
826 \[1061/ \\(ASCE\\) 1090-0241 \\(1997\\) 123:1 \\(9.\]\(https://doi.org/10.1061/\(ASCE\)1090-0241\(1997\)123:1\(9\)](https://doi.org/10.1061/(ASCE)1090-0241(1997)123:1(9)

- 
- 827 Jeng, D.S., Ye, J.H., Zhang, J.S., Liu, P.F., 2013. An integrated model for the wave-induced  
828 seabed response around marine structures: Model verifications and applications. *Coastal En-*  
829 *gineering* 72, 1–19. doi:[https://doi.org/10.1016/j.coastaleng.2012.08.](https://doi.org/10.1016/j.coastaleng.2012.08.006)  
830 006.
- 831 Karunarthna, S., Lin, P., 2006. Numerical simulation of wave damping over porous  
832 seabeds. *Coastal Engineering* 53, 845–855. doi:[https://doi.org/10.1016/j.](https://doi.org/10.1016/j.coastaleng.2006.05.003)  
833 [coastaleng.2006.05.003](https://doi.org/10.1016/j.coastaleng.2006.05.003).
- 834 Kitano, T., Mase, H., 1999. Boundary-layer theory for anisotropic seabed response to sea  
835 waves. *Journal of Waterway, Port, Coastal, and Ocean Engineering*, ASCE 125, 187–194.  
836 doi:[https://doi.org/10.1061/\(ASCE\)0733-950X\(1999\)125:4\(187\)](https://doi.org/10.1061/(ASCE)0733-950X(1999)125:4(187)).
- 837 Lee, T.L., Tsai, C.P., D-S, J., 2002. Ocean waves propagating over a coulomb-damped poroe-  
838 lastic seabed of finite thickness: An analytical solution. *Computers and Geotechnics* 29,  
839 119–149. doi:[http://dx.doi.org/10.1016/S0266-352X\(01\)00024-6](http://dx.doi.org/10.1016/S0266-352X(01)00024-6).
- 840 Li, X., Gao, F., Yang, B., Zang, J., 2011. Wave-induced pore pressure response and soil lique-  
841 faction around pile foundation. *International Journal of Offshore and Polar Engineering* 21,  
842 233–239.
- 843 Li, Y., Ong, M.C., Fuhrman, D.R., 2020a. CFD investigations of scour beneath a submarine  
844 pipeline with the effect of upward seepage. *Coastal Engineering* 156, 103624. doi:[https:](https://doi.org/10.1016/j.coastaleng.2019.103624)  
845 [//doi.org/10.1016/j.coastaleng.2019.103624](https://doi.org/10.1016/j.coastaleng.2019.103624).
- 846 Li, Y., Ong, M.C., Tang, T., 2018. Numerical analysis of wave-induced poro-elastic seabed  
847 response around a hexagonal gravity-based offshore foundation. *Coastal Engineering* 136,  
848 81–95. doi:[10.1016/j.coastaleng.2018.02.005](https://doi.org/10.1016/j.coastaleng.2018.02.005).
- 849 Li, Y.Z., Ong, M.C., Tang, T., 2020b. A numerical toolbox for wave-induced seabed response  
850 analysis around marine structures in the openfoam framework. *Ocean Engineering* 195,  
851 106678. doi:<https://doi.org/10.1016/j.coastaleng.2019.103624>.
- 852 Liang, Z., Jeng, D.S., 2021. Poro-fssi-foam model for seafloor liquefaction around a pipeline

---

853 under combined random wave and current loading. *Applied Ocean Research* 107, 102497.  
854 doi:<https://doi.org/10.1016/j.apor.2020.102497>.

855 Liang, Z., Jeng, D.S., Liu, J., 2020. Combined wave–current induced seabed liquefac-  
856 tion around buried pipelines: Design of a trench layer. *Ocean Engineering* 212, 107764.  
857 doi:[10.1016/j.oceaneng.2020.107764](https://doi.org/10.1016/j.oceaneng.2020.107764).

858 Lin, J., Zhang, J., Sun, K., Wei, X.L., Guo, Y.K., 2020. Numerical analysis of seabed dynamic  
859 response in vicinity of mono-pile under wave-current loading. *Water Science and Engineer-*  
860 *ing* 13, 74–82. doi:<https://doi.org/10.1016/j.wse.2020.02.001>.

861 Lin, Z., Pokrajac, D., Guo, Y., Jeng, D.s., Tang, T., Rey, N., Zheng, J., Zhang, J., 2017. Inves-  
862 tigation of nonlinear wave-induced seabed response around mono-pile foundation. *Coastal*  
863 *Engineering* 121, 197–211. doi:[10.1016/j.coastaleng.2017.01.002](https://doi.org/10.1016/j.coastaleng.2017.01.002).

864 Liu, B., Jeng, D.S., Ye, G.L., Yang, B., 2015. Laboratory study for pore pressures in  
865 sandy deposit under wave loading. *Ocean Engineering* 106, 207–219. doi:[10.1016/j.oceaneng.2015.06.029](https://doi.org/10.1016/j.oceaneng.2015.06.029).

867 Liu, X., Garcia, M.H., 2007. Numerical investigation of seabed response under waves with  
868 free-surface water flow. *International Journal of Offshore and Polar Engineering* 17, 97–104.

869 Liu, X., Zhang, H., Zheng, J., Guo, L., Jia, Y., Bian, C., Li, M., Ma, L., Zhang, S., 2020.  
870 Critical role of wave–seabed interactions in the extensive erosion of Yellow River estuar-  
871 ine sediments. *Marine Geology* 426, 106208. doi:<https://doi.org/10.1016/j.margeo.2020.106208>.

873 Lube, G., Huppert, H.E., Sparks, R.S.J., Hallworth, M.A., 2004. Axisymmetric col-  
874 lapses of granular columns. *Journal of Fluid Mechanics* 508, 175–199. doi:[10.1017/S0022112004009036](https://doi.org/10.1017/S0022112004009036).

876 Madsen, O.S., 1978. Wave-induced pore pressures and effective stresses in a porous bed.  
877 *Géotechnique* 28, 377–393. doi:[10.1680/geot.1978.28.4.377](https://doi.org/10.1680/geot.1978.28.4.377).

878 Mei, C.C., Foda, M.A., 1981. Wave-induced response in a fluid-filled poro-elastic solid with a  
879 free surface—a boundary layer theory. *Geophysical Journal of the Royal Astronomical Society*

---

880 66, 597–631. doi:[https://doi.org/10.1111/j.1365-246X.1981.tb04892.](https://doi.org/10.1111/j.1365-246X.1981.tb04892.x)  
881 [x](#).

882 Shields, A., 1937. Application of similitude mechanics and research on turbulence to bed load  
883 movement. Technical Report 26. Mitteilungender Preussischer Versuchsanstalt für Wasserbau  
884 und Schiffbau.

885 Soulsby, R., 1997. Dynamics of Marine Sands. Thomas Telford, London.

886 Sumer, B.M., 2014. Liquefaction around Marine Structures. World Scientific, New Jersey.

887 Sumer, B.M., Fredsøe, J., 2002. The Mechanics of Scour in the Marine Environment. World  
888 Scientific.

889 Tang, T., Hededal, O., Cardiff, P., 2015. On finite volume method implementation of pro-  
890 elasto-plasticity soil model. International Journal for Numerical and Analytical Methods in  
891 Geomechanics 39, 1410–1430. doi:<https://doi.org/10.1002/nag.2361>.

892 Tsai, C.P., 1995. Wave-induced liquefaction potential in a porous seabed in front of  
893 a breakwater. Ocean Engineering 22, 1–18. doi:[https://doi.org/10.1016/  
894 0029-8018\(94\)00042-5](https://doi.org/10.1016/0029-8018(94)00042-5).

895 Ulker, M.B.C., Rahman, M.S., Jeng, D.S., 2009. Wave-induced response of seabed: various  
896 formulations and their applicability. Applied Ocean Research 31, 12–24. doi:[10.1016/j.  
897 apor.2009.03.003](https://doi.org/10.1016/j.apor.2009.03.003).

898 Verruijt, A., 1969. Elastic storage of aquifers, in: De Wiest, R.J.M. (Ed.), Flow through Porous  
899 Media. Academic Press, pp. 331–376.

900 Wang, J.G., Nogami, T., Dasari, G.R., Lin, P.Z., 2004. A weak coupling algorithm for seabed-  
901 wave interaction analysis. Computer Methods in Applied Mechanics and Engineering 193,  
902 3935–3956. doi:<https://doi.org/10.1016/j.cma.2004.02.011>.

903 Wang, X.X., Jeng, D.S., Tsai, C.C., 2019. Meshfree model for wave-seabed interactions around  
904 offshore pipelines. Journal of Marine Science and Engineering 7, 87. doi:[https://doi.  
905 org/10.3390/jmse7040087](https://doi.org/10.3390/jmse7040087).

- 
- 906 Wen, F., Jeng, D.S., Wang, J., Zhou, X., 2012. Numerical modeling of response of a saturated  
907 porous seabed around an offshore pipeline considering non-linear wave and current inter-  
908 action. *Applied Ocean Research* 35, 25–37. doi:[http://dx.doi.org/10.1016/j.  
909 apor.2011.12.005](http://dx.doi.org/10.1016/j.apor.2011.12.005).
- 910 Yamamoto, T., Koning, H., Sellmeijer, H., Hijum, E.V., 1978. On the response of a poro-  
911 elastic bed to water waves. *Journal of Fluid Mechanics* 87, 193–206. doi:[10.1017/  
912 S0022112078003006](https://doi.org/10.1017/S0022112078003006).
- 913 Yang, G., Ye, J.H., 2017. Wave & current-induced progressive liquefaction in loosely de-  
914 posited seabed. *Ocean Engineering* 142, 303–314. doi:[https://doi.org/10.1016/  
915 j.oceaneng.2017.07.027](https://doi.org/10.1016/j.oceaneng.2017.07.027).
- 916 Ye, J., He, K., Zhou, L., 2021. Subsidence prediction of a rubble mound breakwater at yantai  
917 port: A application of FSSI-CAS 2D. *Ocean Engineering* 219, 108349. doi:[https://  
918 doi.org/10.1016/j.oceaneng.2020.108349](https://doi.org/10.1016/j.oceaneng.2020.108349).
- 919 Ye, J., Jeng, D.S., 2011. Effects of bottom shear stresses on the wave-induced dynamic response  
920 in a porous seabed: Poro-wssi (shear) model. *Acta Mechanica Sinica* 27, 898–911. doi:[10.  
921 1007/s10409-011-0469-1](https://doi.org/10.1007/s10409-011-0469-1).
- 922 Ye, J., Jeng, D.S., 2012. Response of seabed to natural loadin:: waves and current. *Journal of*  
923 *Engineering Mechanics, ASCE* 138, 601–613. doi:[10.1061/\(ASCE\)EM.1943-7889.  
924 0000356](https://doi.org/10.1061/(ASCE)EM.1943-7889.0000356).
- 925 Ye, J., Jeng, D.S., Chan, A.H.C., Wang, R., Zhu, Q.C., 2016. 3D integrated numerical model  
926 for fluid–structures–seabed interaction (fssi): Elastic dense seabed foundation. *Ocean En-*  
927 *gineering* 115, 107–122. doi:[http://dx.doi.org/10.1016/j.oceaneng.2016.  
928 01.003](http://dx.doi.org/10.1016/j.oceaneng.2016.01.003).
- 929 Ye, J., Jeng, D.s., Wang, R., Zhu, C., 2015. Numerical simulation of the wave-induced dy-  
930 namic response of poro-elastoplastic seabed foundations and a composite breakwater. *Ap-*  
931 *plied Mathematical Modelling* 39, 322–347. doi:[10.1016/j.apm.2014.05.031](https://doi.org/10.1016/j.apm.2014.05.031).

- 
- 932 Ye, J., Zhang, Y., Wang, R., Zhu, C., 2014. Nonlinear interaction between wave, breakwa-  
933 ter and its loose seabed foundation: A small-scale case. *Ocean Engineering* 91, 300–315.  
934 doi:<https://doi.org/10.1016/j.oceaneng.2014.09.003>.
- 935 Zhang, J.S., Jeng, D.S., Liu, P.F., 2011. Numerical study for waves propagating over a porous  
936 seabed around a submerged permeable breakwater: PORO–WSSI II model. *Ocean Engineer-*  
937 *ing* 38, 954–966. doi:[10.1016/j.oceaneng.2010.10.018](https://doi.org/10.1016/j.oceaneng.2010.10.018).
- 938 Zhang, Q., Hisada, T., 2001. Investigations of the coupling methods for FSI analysis by FEM.  
939 *Trans. Japan. Soc. Mech. Eng.* 67, 1555–1562.
- 940 Zhao, H.Y., Jeng, D.S., 2015. Numerical study of wave-induced soil response in a sloping  
941 seabed in the vicinity of a breakwater. *Applied Ocean Research* 51, 204–221. doi:<http://dx.doi.org/10.1016/j.apor.2015.04.008>.
- 942
- 943 Zhao, H.Y., Zhu, J.F., Zheng, J.H., Zhang, J.S., 2020. Numerical modelling of the fluid–seabed–  
944 structure interactions considering the impact of principal stress axes rotations. *Soil Dynam-*  
945 *ics and Earthquake Engineering* 136, 106242. doi:[https://doi.org/10.1016/j.](https://doi.org/10.1016/j.soildyn.2020.106242)  
946 [soildyn.2020.106242](https://doi.org/10.1016/j.soildyn.2020.106242).

#### 947 **Appendix A. Code of two-way coupling method for wave and seabed model**

948 In this study, based on the previous OpenFOAM model (PORO-FSSI-FOAM, [Liang et al.](#)  
949 [\(2020\)](#)), we modify the program by including the concept of two-way coupling process. The  
950 code for the new component regarding the two-way coupling method is provided for readers to  
951 use. The numerical model can be directly used for both small-scale or large scale numerical  
952 simulations for various marine infrastructures for evaluation of the seabed response around a  
953 marine structure. If the readers would like to use the present model, they can directly use it  
954 or modify for their own purposes. Certainly, they need to have the basic knowledge of using  
955 OpenFOAM. We added some notes in the codes to help readers understand our code. If the  
956 readers who have no experience with numerical modelling in OpenFOAM, they can contact the  
957 authors for additional help.

```
#include "fvCFD.H"
```

---

```

#include "dynamicFvMesh.H"
#include "CMULES"
#include "EulerDdtScheme.H"
#include "localEulerDdtScheme.H"
#include "subCycle.H"
#include "miscibleIncompressibleTwoPhaseMixture.H"
#include "kinematicMomentumTransportModel.H"
#include "pimpleControl.H"
#include "fvOptions.H"
#include "CorrectPhi.H"
#include "fvcSmooth.H"
#include "primitivePatchInterpolation.H"
/** The basic header file for the RANS wave model and QS seabed model. */
int main(int argc, char *argv[])
{
#include "olaFlow.H"
/** The header file to solve the RANS equation in Section 2.2, which can be obtained from
Higuera et al. (2013). */
label patchWallID = mesh.boundaryMesh().findPatchID("bottom");
label patchWallID1 = mesh.boundaryMesh().findPatchID("seabed");
/** The path ID of "bottom" and "seabed", which are the bottom of flow model and the surface
of seabed model. */
vectorField Point1 = mesh.boundaryMesh() [patchWallID].faceCentres();
scalarField Point1z = Point1.component(2);
/** The z- coordinates of mesh face center for the bottom boundary. */
int p1size = Point1z.size();
scalar sum = 0;
forAll(Point1z, index)
{ sum =sum + Point1z[index]; }
scalar z1 = sum / p1size;

```

---

```

/** Calculate the average value of z- coordinates for the bottom boundary. */
vectorField Point2 = mesh.boundaryMesh() [patchWallID1].faceCentres();
scalarField Point2z = Point2.component(2);
int p2size = Point1z.size();
scalar sum1 = 0;
forAll(Point2z, index)
{ sum1 =sum1 + Point2z[index]; }
scalar z2 = sum1 / p2size;
/** Calculate the average value of z- coordinates for the seabed boundary. */
scalarField ppoint(p2size);
if ((p1size) = (p2size) )
{ ppoint = p_rgh.boundaryFieldRef()[patchWallID]; }
/** If the mesh number of bottom and surface boundaries are same, the hydrodynamic water
pressure at the bottom boundary are put on the scalar Field of "ppoint". */
else
{
vectorField Point3(p2size);
forAll(Point3, index)
{
Point3[index].x() = Point2[index].x();
Point3[index].y() = Point2[index].y();
Point3[index].z() = Point2[index].z() + (z1 - z2);
}
interpolationCellPoint < scalar > pInterpolate(p_rgh);
forAll(Point3, index)
{
label cellID = mesh.findCell(Point3[index]);
scalar pInterp = pInterpolate.interpolate(Point3[index], cellID);
ppoint[index] = pInterp;
}

```

---

```
}
```

```
/** If the mesh number of bottom and surface boundaries are different, the hydrodynamic water pressure at the bottom boundary interpolate to the grid center of the seabed boundary to "ppoint". **/
```

```
ps.boundaryFieldRef()[patchWallID1] == ppoint;
```

```
/** Replace the value of pore-pressure at the seabed boundary by using the hydrodynamic water pressure at the bottom boundary. **/
```

```
#include "DONG-OF4-SEABED-FOAM.H"
```

```
/** The header file to solve the QS equation in Section 2.3, which can be obtained from
```

```
Liang et al. \(2020\). **/
```

```
volVectorField Vs1
```

```
(
```

```
IOobject
```

```
(
```

```
"Vs1",
```

```
runTime.timeName(),
```

```
mesh,
```

```
IOobject::MUST_READ,
```

```
IOobject::AUTO_WRITE
```

```
),
```

```
-(ks/rhow/mag(g))*ns*fvc::grad(ps)
```

```
);
```

```
/** Establish the seepage induced velocity field **/
```

```
volVectorField Vs2
```

```
(
```

```
IOobject
```

```
(
```

```
"Vs1",
```

```
runTime.timeName(),
```

```
mesh,
```

```
IOobject::MUST_READ,
```

---

IObject::AUTO\_WRITE

),

(1-ns)\*fvc::ddt(Us)

);

**/\*\* Establish the soil displacement induced velocity field \*/**

if ((p1size) = (p2size) )

{

vectorField Vs1seabed = Vs1.boundaryFieldRef()[patchWallID1];

vectorField Vs2seabed = Vs2.boundaryFieldRef()[patchWallID1];

vectorField Vsseabed = Vs1seabed + Vs2seabed;

}

**/\*\* If the mesh number of bottom and surface boundaries are same, the flow velocity at the surface boundary are put on the vector field of "Vsseabed". \*/**

else

{

vectorField Point4(p1size);

forAll(Point4, index)

{

Point4[index].x() = Point1[index].x();

Point4[index].y() = Point1[index].y();

Point4[index].z() = Point1[index].z() + (z2 - z1);

}

interpolationCellPoint < vector > Vs1Interpolate(Vs1);

interpolationCellPoint < vector > Vs2Interpolate(Vs2);

forAll(Point4, index)

{

label cellID = mesh.findCell(Point4[index]);

vector Vs1Interp = Vs1Interpolate.interpolate(Point4[index], cellID);

vector Vs2Interp = Vs2Interpolate.interpolate(Point4[index], cellID);

Vsseabed[index] = Vs1Interp + Vs2Interp;

---

```
}
```

```
}
```

```
/** If the mesh number of bottom and surface boundaries are different, the flow velocity at the surface boundary interpolate to the face center of the seabed boundary to "Vsseabed". **/
```

```
U.boundaryFieldRef()[patchWall] == Vsseabed;
```

```
/** Replace the value of flow velocity at the bottom boundary by using the seepage and soil displacement induced velocity at the surface boundary. **/
```

```
return 0;
```

```
}
```